View metadata, citation and similar papers at core.ac.uk

brought to you by CORE

provided by University of Central Florida (UCF): STARS (Showcase of Text, Archives, Research &...

STARS

University of Central Florida

STARS

Electronic Theses and Dissertations, 2004-2019

2007

Investigation Of Pn Junction Delineation Resolution Using Electron Beam Induced Current

Christopher Hayden Hontgas

University of Central Florida

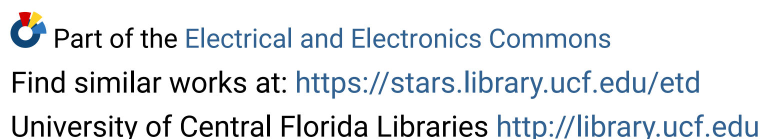

Part of the Electrical and Electronics Commons

Find similar works at: https://stars.library.ucf.edu/etd

University of Central Florida Libraries http://library.ucf.edu

This Doctoral Dissertation (Open Access) is brought to you for free and open access by STARS. It has been accepted for inclusion in Electronic Theses and Dissertations, 2004-2019 by an authorized administrator of STARS. For more information, please contact STARS@ucf.edu.

STARS Citation

Hontgas, Christopher Hayden, "Investigation Of Pn Junction Delineation Resolution Using Electron Beam Induced Current" (2007). *Electronic Theses and Dissertations, 2004-2019*. 3208.
https://stars.library.ucf.edu/etd/3208

INVESTIGATION OF PN JUNCTION DELINEATION RESOLUTION USING ELECTRON BEAM INDUCED CURRENT

by

CHRISTOPHER HAYDEN HONTGAS
M.S.E.E. Auburn University, 1998
B.S. James Madison University, 1984

A dissertation submitted in partial fulfillment of the requirements
for the degree of Doctor of Philosophy
in the School of Electrical Engineering and Computer Science
in the College of Engineering and Computer Science
at the University of Central Florida
Orlando, Florida

Fall Term
2007

Major Professor: Donald C. Malocha

© 2007 Hayden Hontgas

ABSTRACT

This dissertation will investigate electron beam induced current (EBIC) for determining semiconductor material and device parameters. While previous experimental work on PN junction delineation using EBIC with the scanning electron microscope has resulted in resolution to approximately 10 nm, theoretical study shows the potential use of EBIC for higher resolution (nanometer) PN junction and FET channel length delineation using the transmission electron microscope. Theoretical arguments using computer simulations of electron beam generation volume, collection probability and EBIC were performed and are presented for the purpose of determining EBIC use in a 300 keV transmission electron microscope (TEM) for PN junction depth determination. Measured results indicate that by measuring thin semiconductor samples with high surface recombination velocity and by using a narrow, high-energy electron beam in the STEM mode of a transmission electron microscope, nanometer resolution may be possible. The practical and experimental limits of beam energy and semiconducting material thermal damage will be discussed.

ACKNOWLEDGMENTS

The author thanks Dr. Wilbur C. Bigelow, Professor Emeritus, Materials Science and Engineering, University of Michigan for fabrication of electron microscope specimen holders and for many useful discussions.

TABLE OF CONTENTS

LIST OF FIGURES vi

LIST OF TABLES ix

LIST OF ACRONYMS/ABBREVIATIONS x

CHAPTER ONE: INTRODUCTION 1

CHAPTER TWO: THEORY 7

CHAPTER THREE: EXPERIMENTAL METHODS 23

CHAPTER FOUR: RESULTS 35

CHAPTER 5: DISCUSSION and CONCLUSIONS 46

Appendix A 51

LIST OF REFERENCES 57

LIST OF FIGURES

Figure 1. Two common EBIC specimen geometries. 2

Figure 2. Electron and hole carrier mechanism with impinging electron beam, no surface recombination. 2

Figure 3. Electron and hole carrier mechanism with impinging electron beam, with surface recombination. 3

Figure 4. EBIC specimen prepared in a beveled geometry [35]. 5

Figure 5. Doping concentration within the SCR. 7

Figure 6. Electric field within a graded PN junction (SCR). 9

Figure 7. Collection probability versus source depth, z, for a point source. x - xscr = 5, 100, 200, 300, 400, 500 nm, respectively, starting with top most curve. 11

Figure 8. EBIC specimen geometry and coordinate system used for simulation. 12

Figure 9. Carrier generation contour plot for 300 keV beam energy, z – axis is normal to specimen surface, x – axis is the lateral distance from point of e-beam injection. 15

Figure 10. Carrier generation contour plot for E_b = 300 keV beam from x = -0.1 to 0.1 µm, z = 0 to 1 µm. 16

Figure 11. Carrier generation contour plot of significant region, as defined in text. 17

Figure 12. EBIC signal, I(Xo), versus surface recombination velocity, s, for sample thickness of d = 10 Lb. 20

Figure 13. EBIC signal, I(Xo), versus surface recombination velocity, s, for sample thickness of d= 1 Lb. 21

Figure 14. EBIC signal, I(Xo), versus surface recombination velocity, s, for sample thickness of d = 0.1Lb. 22
Figure 15. Specimen holder for EBIC measurements which allows electrical contact between specimen and microscope electronics.. 23
Figure 16. Stanford Research Systems Model SR570 Low-Noise Current Amplifier. 25
Figure 17. FEI Tecnai F30 TEM. (Photo courtesy of FEI company). 26
Figure 18. Typical EBIC measurement configuration. 27
Figure 19. Theoretical impurity concentration profile for fabricated diodes. 32
Figure 20. Final theoretical dopant profile, Nd(x) - Na. 33
Figure 21. Typical EBIC specimen geometry used in this study. 33
Figure 22. Typical I-V curve for a EBIC specimen diode. 34
Figure 23. EBIC measurement signal flow. 36
Figure 24. Two dimensional contrast image on left, EBIC image top right, EBIC line scan profile bottom right. 37
Figure 25. EBIC line scan from contrast image. 38
Figure 26. Typical TEM contrast image. Figure 27. Typical EBIC image. 39
Figure 28. Contrast image of diode tip. Figure 29. EBIC image of diode tip. 40
Figure 30. EBIC signal versus diode thickness. 41
Figure 31. Graph showing EBIC signal versus specimen thickness. 41
Figure 32. EBIC peak width (95%) versus line scan position from wedge tip. 42
Figure 33. Contrast image (left) and EBIC image (right). 43
Figure 34. Close-up of damage due to line scan. 44

Figure 35. Image enhanced to show narrowing of EBIC profile in damaged region along line scan. 45

Figure 36. EBIC image showing line scan location. 46

Figure 37. Data from line scan of Figure 33. 47

Figure 38. Pixel pitch versus magnification. 48

Figure 39. STEM spatial calibration grid pattern. 49

LIST OF TABLES

Table 1. Parameters and values used in simulation. 12

Table 2. Process schedule for diode fabrication. 28

Table 3. Process schedule for firing conductive film. 28

Table 4. Low-noise current amplifier settings. 35

Table 5. TEM settings. 35

LIST OF ACRONYMS/ABBREVIATIONS

EBIC	Electron Beam Induced Current
EHP	Electron-Hole Pair
FET	Field Effect Transistor
SCR	Space Charge Region
STEM	Scanning Transmission Electron Microscopy
TEM	Transmission Electron Microscopy

CHAPTER ONE: INTRODUCTION

For many years the current induced by an impinging electron beam close to a PN semiconductor junction has been used to determine the bulk diffusion length, minority carrier lifetime, surface recombination velocity, analyze crystal dislocations, and to locate a PN junction [1]-[43]. The electron beam induced current (EBIC) mode of the scanning electron microscope (SEM) is used for these measurements with beam energies of 10-40 keV.

Continued scaling of semiconductor devices has challenged existing measurement techniques for channel length and PN junction delineation. Determination of a PN junction location in semiconductor devices to nanometer resolution through EBIC measurement has been investigated in previous studies [44], [45]. Spatial resolution to 10 nm from EBIC measurement using beveled samples has been reported in the literature [44]. Limiting factors include beam-sample interaction, carrier re-distribution, sample geometry, minority carrier diffusion length and others [45].

For EBIC measurements the electron beam impinges perpendicularly to the semiconductor surface and is moved toward the PN junction while the induced current is measured. Two typical PN junction geometries used are the planar and parallel junctions as shown in Fig. 1. The focus of this research is to investigate silicon PN junction location with a TEM and the parallel geometry shown in Fig.1(b).

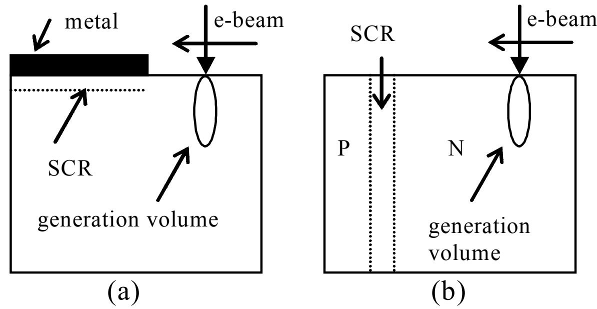

Figure 1. Two common EBIC specimen geometries.

The e-beam from the microscope creates an electron-hole pair generation volume within the semiconductor sample. In the absence of surface recombination these carriers will diffuse out from the generation volume. The case of the e-beam impinging on the p-side of a PN junction will be discussed as depicted in Figure 2.

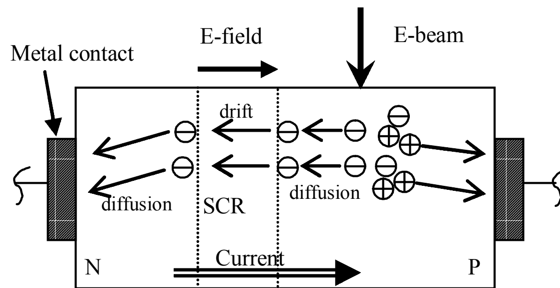

Figure 2. Electron and hole carrier mechanism with impinging electron beam, no surface recombination.

Electrons diffusing to the SCR will drift across the SCR to the n-side due to the built-in electric field. These electrons diffuse and are collected at the ohmic contact. An equivalent number of holes recombine with electrons at the ohmic contact on the p-side resulting in EBIC. An

equivalent explanation can be made for the e-beam impinging on the n-side. Both cases result in an induced current from the p-side to n-side.

In the case where significant surface recombination, v_s, exists, and the generation volume is close to the semiconductor surface with respect to the bulk minority carrier diffusion length, L_b, the induced EBIC is reduced. Figure 3 displays this effect. Some carriers that may have contributed to the measured EBIC recombine at the semiconductor surface and the measured EBIC is lower than if no surface recombination existed. As the generation volume comes closer to the SCR edge, the diffusion of carriers to the SCR edge becomes more significant than the diffusion to the surface.

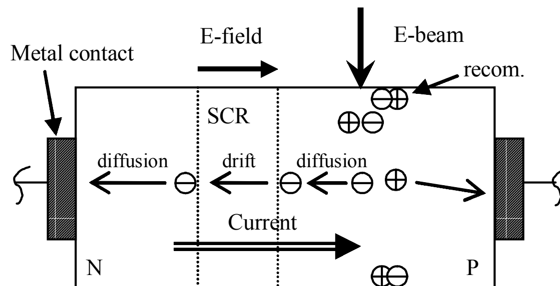

Figure 3. Electron and hole carrier mechanism with impinging electron beam, with surface recombination.

The EBIC will increase and then peak when the generation volume is in the SCR. The sharpness of this EBIC profile will increase with increasing v_s.

The carrier generation volume created by the impinging electron beam decreases with decreasing beam energy. Previous work has suggested this approach to increasing resolution [30], [43]. Indeed, lowering the electron beam energy will result in increased resolution. Ideally

a generation volume "point source" would be used, but this is physically unrealizable. Additionally, the beam energy must be large enough to create a generation volume that produces an EBIC above the noise level of the measuring instrumentation. Thus a measurement, and therefore resolution, is limited as beam energy decreases.

For a sample with large L_b, the induced current profile, as a function of distance from the PN junction is expected to be broad. This is due to minority carriers reaching the built-in electric field in the space charge region and drifting across to the majority carrier region when the beam is within a diffusion length of the junction. Given a sample with high surface recombination velocity, v_s, carriers within a diffusion length of the surface recombine at the surface rather than diffuse to the space charge region when the beam is away from the PN junction. Once close to the PN junction, diffusion to and drift across the SCR becomes comparable to surface recombination resulting in increased EBIC. This EBIC signal should become steeper near and peak at the SCR, resulting in an overall narrowing of the profile thus providing increased resolution.

The approach discussed above has been successfully explored in previous work [35]. High surface recombination velocity to 20,000 cm/sec for silicon has been produced through various sample preparation techniques, such as surface passivation followed by oxide growth, ion beam milling, electron bombardment, and surface abrasion [37], [38]. Well-polished 10 Ω-cm p-type and 5 Ω-cm n-type silicon have $v_s \sim 10^4$ cm/sec. The same sample with abraded (lapped) surfaces have $v_s \sim 10^7$ cm/sec [37]. Surface passivation techniques are used to reduce v_s. Immersion in HF, iodine/ethanol, iodine and bromine have resulted in v_s values of approximately 0.25, 10, 4, and 20 cm/sec, respectively [46].

Ion beam milling can be used to sputter off layers of a silicon surface. The ion milling damages the surface to a depth of a few nanometers when a beam angle of 15° is used. Minority carrier lifetimes, τ_s, due to the damaged surface have been reported to be less than 10^{-15} sec, resulting in high v_s [46].

EBIC measurement on beveled samples with high v_s has shown promise [44]. The geometry for this approach is shown in Figure 4. A beveled surface causes a "deformation/reducing" of the SCR at the surface. It is believed the lower part of the SCR is reduced due to the missing ionized dopants in the upper side of the SCR.

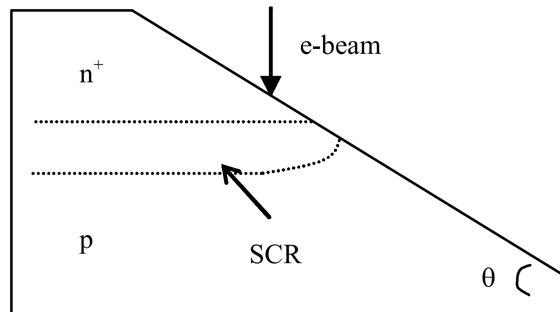

Figure 4. EBIC specimen prepared in a beveled geometry [35].

Also, the bevel angle, θ, was shown to be critical with the best resolution at θ = 0.91°. A thin surface oxidation was performed and the surface was bombarded with a 5 keV, 100nA scanning electron beam for 120 min, creating a high and stable v_s. Junction resolution to 10 nm was achieved in this work [44].

Work performed by Kittler [44] relies on bevel angle and the deformation of the SCR. The research proposed here will study analytically and experimentally the effect on EBIC of thin diode samples with high surface recombination velocity. A preferred specimen structure and

geometry are developed. Also it will be shown that by using a high (300keV) beam energy to probe a thin sample with high v_s on both surfaces, the diffusion to the surface and subsequent recombination can produce a sharpening of the EBIC, however resolution is limited by the thermal heating and therefore damage to the semiconducting material at this high beam energy. These items are presently not in the literature.

CHAPTER TWO: THEORY

In this research, PN junctions were produced by thermal diffusion of a dopant into a uniformly doped silicon substrate. The resultant dopant profile within a narrow range within the metallurgical junction is approximately linear [46]. Using this approximation a 1-D expression for the electric field in the SCR is derived and plotted.

One begins with Poisson's equation:

$$\vec{\nabla} \bullet \vec{E}(x) = \frac{\rho}{\varepsilon} \tag{1}$$

Considering a uniformly doped p-type semiconductor with donor dopants thermally diffused into it, the dopant concentration within the SCR can be approximated as a linear function as shown in Figure 5.

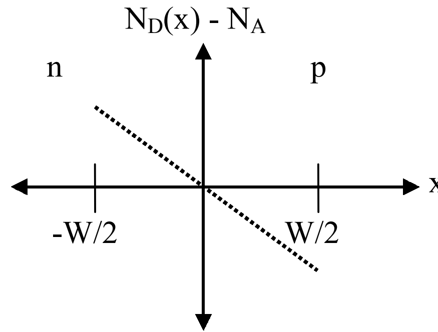

Figure 5. Doping concentration within the SCR.

In general the charge density inside a semiconductor is given by:

$$\rho = q(p - n + N_D - N_A) \tag{2}$$

where q = elemental charge (coulomb/second), p = density of holes in the valence band (holes/cm^3), n = density of electrons in the conduction band (electrons/cm^3), N_D = density of ionized donor dopants (donor dopants/cm^3), and N_A = density of ionized acceptor dopants (acceptor dopants/cm^3). Inside the SCR the density of electrons and holes is negligible compared to the density of ionized dopants. Therefore, for this case where the ionized donor dopant concentration is a function of x:

$$\rho \cong q(N_d(x) - N_A) \tag{3}$$

Equation (1) becomes:

$$E(x) = \int_0^{E(x)} dE = \int_{-\frac{W}{2}}^{x} \frac{\rho}{\varepsilon} dx \tag{4}$$

The symmetry of the charge density requires that the SCR will be of equal width on either side of the metallurgical junction. By comparing Figure 1 with equation (3) an equation for ρ as a function of x can be assumed. Let $\rho = -qax$, where a (cm^{-4}) is an experimentally determined grading constant. Equation (4) now becomes:

$$E(x) = -\frac{qa}{\varepsilon} \int_{-\frac{W}{2}}^{x} x dx . \tag{5}$$

The electric field is found to be:

$$E(x) = -\left[\frac{qa}{2K_s \varepsilon_o}\right] \times \left[x^2 - \left(\frac{w}{2}\right)^2\right] \tag{6}$$

where K_s is the relative permittivity of silicon (11.8) and ε_o is the permittivity of free space, W is the SCR width.

Figure 6 shows a 1-D plot of the electric field for a linearly graded junction with W calculated to be 0.7036 μm and maximum electric field strength (at x = 0) to be 6.863×10^3 volt/cm. The grading constant, $a = 7.234 \times 10^{19}$ cm^{-4}, was taken from the impurity concentration profile calculated from the process parameters for the diodes fabricated for this research (see Figure 19).

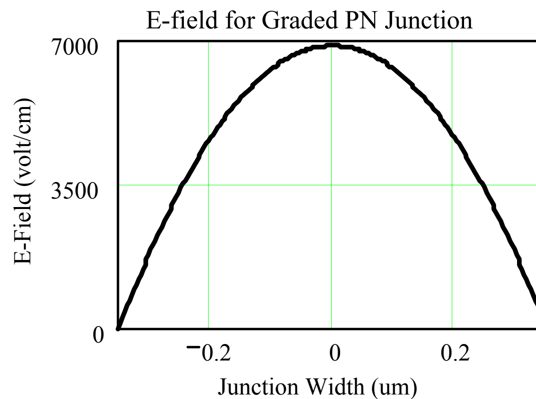

Figure 6. Electric field within a graded PN junction (SCR).

This shows the parabolic form of the electric field centered about x = 0, the metallurgical junction. Since the EBIC is due to the drift of carriers across the SCR it is expected that the EBIC peak will occur when the generation volume is completely within the SCR. Thus the peak of the EBIC profile will coincide with the location of the maximum value of the electric field, which is expected to be at the SCR center.

The collection efficiency for a point generation source as a function of distance, x, from the SCR is given by [47]:

$$P(x) = \exp\left(\frac{-(x - x_{scr})}{L_b}\right) - \left(\frac{2}{\pi}\right) \times \int_0^\infty \frac{k \times \exp\left[-z\left(k^2 + \frac{1}{L_b^2}\right)^{1/2}\right] \times \sin\left[k(x - x_{scr})\right]}{\left(k^2 + \frac{1}{L_b^2}\right) \times \left[\left(\frac{D}{v_s}\right)\left(k^2 + \frac{1}{L_b^2}\right)^{1/2} + 1\right]} dk \qquad (7)$$

where x_{scr} is the location of the SCR, z is the depth of the point source, D is the diffusion coefficient. D is a function of L_b given by the expression:

$$D = \frac{L_b^2}{\tau} \qquad (8)$$

where τ is the minority carrier lifetime. In the limit where $L_b \to \infty$ (no recombination in the bulk material) and $v_s \to \infty$ (all carriers diffusing to the surface recombine at the surface) equation (7) becomes [47][1]:

$$P(x, z) = 1 - \left(\frac{2}{\pi}\right) \arctan\left[\frac{(x - x_{SCR})}{z}\right] \qquad (9)$$

This situation is somewhat applicable for thin solar cell grade silicon with high recombination velocity, but is unrealistic for devices for which this research in intended. Yet, it illustrates the effect of high v_s on EBIC. Equation (4) is plotted in Figure 7 for six different values of $x - x_{scr}$. The upper most curve is for $x - x_{scr} = 5$ nm. The adjacent curves are for 100 nm, 200 nm, 300 nm, 400 nm and 500 nm, respectively. One can see the collection probability is a strong function of not only the beam-to-junction distance but also the beam-to-high v_s surface.

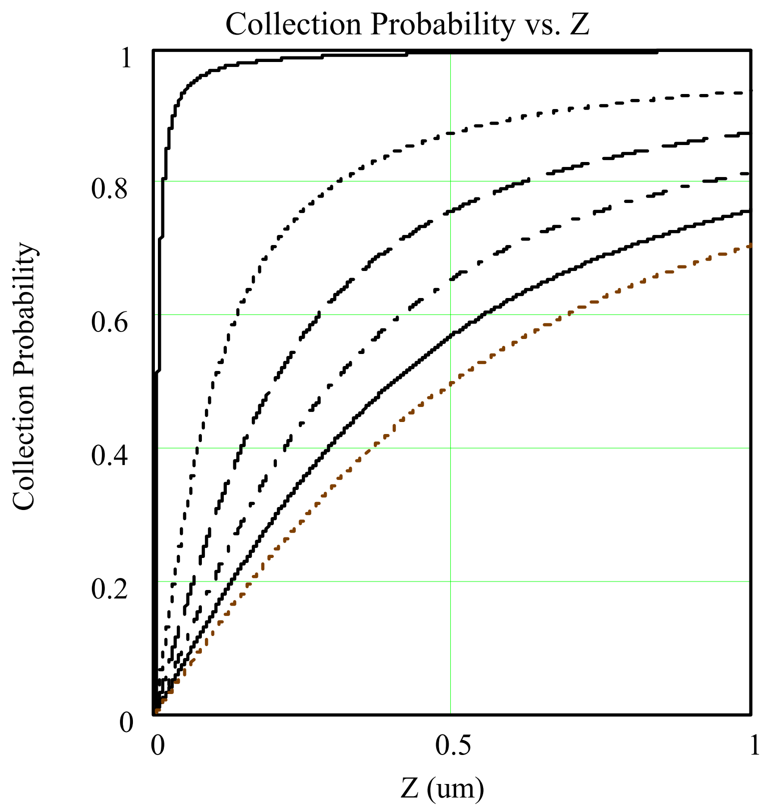

Figure 7. Collection probability versus source depth, z, for a point source. x - xscr = 5, 100, 200, 300, 400, 500 nm, respectively, starting with top most curve.

The extended generation volume due to an electron beam incident on a silicon surface was simulated based on the literature in the field. The geometry of the electron beam relative to a PN junction is shown in Figure 8.

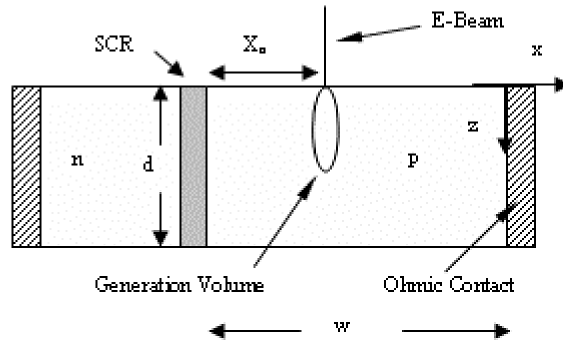

Figure 8. EBIC specimen geometry and coordinate system used for simulation.

In this simulation the material selected was silicon and material parameter values shown in Table 1 are for silicon. Beam parameters in Table 1 are typical of STEM systems. Material thickness of 1.1R and 1 μm were used, where R is the electron penetration depth.

Table 1. Parameters and values used in simulation.

Parameter	**Value**
Electron beam energy, E_b	300 keV
Density of silicon, ρ	2.33 g/cm^3
Energy required for electron/hole pair generation, E_i	3.75 eV
Electron beam current, I_b	0.7 nA
Mean fraction of backscattered energy, f	0.08
Electron beam diameter, d_b	0.5 X 10^{-3} μm

The electron penetration depth in silicon is found by the use of the following expression [48], [49]:

$$R = \left(\frac{3.98 \times 10^{-2}}{\rho} \right) (E_b)^{1.75} \quad (10)$$

This equation is claimed to be sufficiently accurate for beam energies between 20 keV and 200 keV [48]. Using values from Table 1 yields a value of 182 μm for R. As a comparison, R = .02 μm for 1 keV electrons and R = 4.8 μm for 25 keV. The simulated distribution of the generated carriers is approximated by the function [25]:

$$g(x,z) = G_o F(x,z) h(z) \quad (11)$$

where the carrier pair generation rate, G_o, is given by:

$$G_o = \frac{E_b I_b}{q E_i} (1 - f) \quad (12)$$

E_i is defined as the energy required to generate an electron-hole pair, 3.75 eV for silicon [24]. The mean fraction of the backscattered energy (f) is 0.08 [25], and I_b is the beam current, set to 0.7 nA for the simulations.

The radially symmetric distribution of generated carriers as a function of depth is [27]:

$$F(x,z) = \left[\frac{1.76}{2\pi\sigma^2 R} \right] \exp\left(\frac{-x^2}{\sigma^2} \right) \quad (13)$$

where

$$\sigma^2 = 0.36 d_b + 0.11 \frac{z^3}{R} \quad (14)$$

and d_b is the beam diameter. This is a Gaussian distribution normalized to give a spreading of distribution with depth but no change in total generation. Thus, the required depth distribution function, h(z), is given by [25]:

$$h(z) = 0.6 + 6.21\left(\frac{z}{R}\right) - 12.4\left(\frac{z}{R}\right)^2 + 5.69\left(\frac{z}{R}\right)^3 \tag{15}$$

Equation (15) is valid for $1.1R \geq z \geq 0$.

A contour plot of (11) is illustrated in Figure 9 for $0 < z < 1.1R$. This plot shows the shape of the volume using values from Table 1. The outer most contour line corresponds to a "low" g(x,z) magnitude with each adjacent contour line corresponding to a one order of magnitude increase in g(x,z). The generation volume 'mushrooms' as the depth, z, increases and extends laterally (in the x-direction) approximately 450 μm from the beam center. As can be deduced from Figure 9, for a 'thick' sample, meaning a z value on the order of R, the EBIC profile will be broad since current will be measured even when the beam is far from the junction.

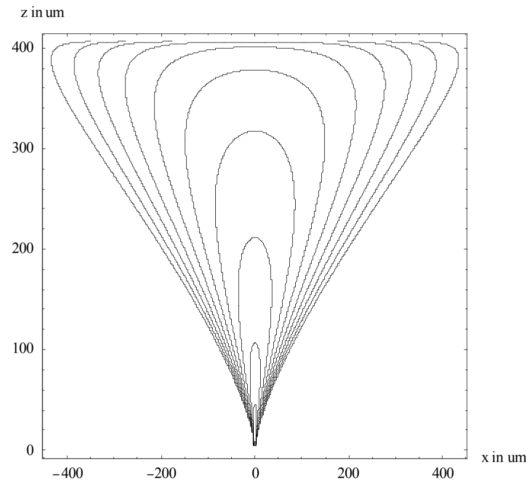

Figure 9. Carrier generation contour plot for 300 keV beam energy, z – axis is normal to specimen surface, x – axis is the lateral distance from point of e-beam injection.

Next, a contour plot of (11) as illustrated in Figure 10 for 0 μm < z < 1 μm was plotted to determine the shape and extent of the generation volume for a silicon sample with a thickness of 1 μm. As before, the outer most contour line corresponds to a "low" g(x,z) magnitude with each adjacent contour line corresponding to a one order of magnitude increase in g(x,z). This shows the effect of a thin sample on the generation volume. For a sample 1 μm thick, the generation volume extends out to approximately 100 μm from the beam center versus 450 μm for a thick sample. This suggests a much narrower EBIC profile will be measured for a thin sample than for a thick sample, thus improving the p-n junction delineation resolution at the expense of total current.

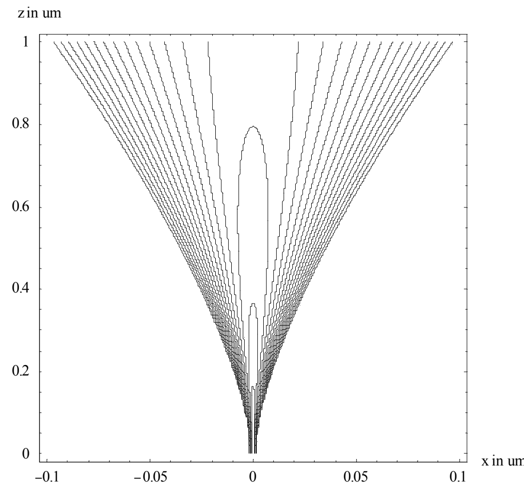

Figure 10. Carrier generation contour plot for E_b = 300 keV beam from x = -0.1 to 0.1 μm, z = 0 to 1 μm.

The low magnitude, outer contour lines show the most spread with increasing z. To establish the contribution to the EBIC of these low magnitude regions is negligible, the 3-D distribution of the generated carriers function [25] was integrated over the $g(r,\theta,z) = 1/(\mu m^2 \cdot s)$, $1\ \mu m \geq z \geq 0\ \mu m$ region to find the total number of carriers, then integrated over decreasing $g(r,\theta,z)$ values until 90% of the total was found. This occurred for the contour line of 6.7×10^{13} per $\mu m^2 \cdot s$, within which the significant portion of the EHP generation volume is contained. Figure 11 is a contour plot of this region for $0\ \mu m < z < 1\ \mu m$, $-1\ \mu m < x < 1\ \mu m$.

As can be seen from Figure 11, the effective, or significant, generation volume can be considered approximately cylindrical, the reasoning behind the delta function representation of the generation volume.

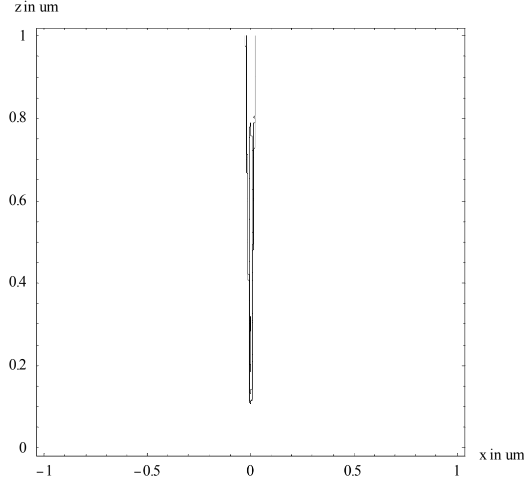

Figure 11. Carrier generation contour plot of significant region, as defined in text.

For thin samples with high energy electron beams, the above discussion indicates the generation volume extends through the specimen with little horizontal spreading. In the limit that the spreading is small in comparison to the effective diffusion length, the approximation is made that the generation volume is a delta function extending through the specimen but with no lateral spread.

Following the study of generation volume in silicon, the effect of surface recombination velocity for thin samples on the total collected current was determined. Again, a model developed in Mathematica was used to determine the beam-induced current as a function of the beam-junction distance.

By the corresponding 2D steady state minority carrier diffusion equation given by Donolato [50]:

$$D\Delta^2 q(x,z) - \frac{1}{\tau} q(x,z) = -h(x,z) \tag{16}$$

where *q(x,z)* is the total excess hole density in x,z space, *D* and τ are the minority carrier diffusion coefficient and minority carrier lifetime, respectively. The function $h(x,z)$ is the generation term described by a delta function.

$$h(x,z) = \delta(x - x') \tag{17}$$

A generic solution of equation (16) is [50]:

$$q(x,z) = \int_0^\infty a(k,z)\sin(kx)dk \tag{18}$$

giving the following after substitution,

$$\int_0^\infty \left[-k^2 a(k,x) + \frac{\partial^2 a(k,x)}{\partial z^2} - \lambda^2 a(k,x) \right] \sin(kx)\partial k = -\frac{2}{\pi D}\int_0^\infty \sin(kx)\sin(kx')\partial k \tag{19}$$

where $\lambda = \dfrac{1}{(D\tau)^{1/2}}$ and the integral representation for the delta function is used,

$$\delta(x - x') = \frac{2}{\pi}\int_0^\infty \sin(kx)\sin(kx')\partial k \tag{20}$$

As can be seen from equation (19), the integral can be taken outside the equation yielding a differential equation that can be easily solved by Mathematica, with the following boundary conditions,

$$\begin{aligned} \left.\frac{\partial a(k,z)}{\partial z}\right|_{z=0} &= s \times a(k,0) \\ \left.\frac{\partial a(k,z)}{\partial z}\right|_{z=d} &= s \times a(k,d) \end{aligned} \tag{21}$$

where $s = \frac{v_s}{D}$, yields the following solution,

$$a(k,z) = \frac{2\left[s\left(1 + e^{\mu d} - e^{\mu(d-z)} - e^{\mu z}\right) - \mu\left(1 - e^{\mu d}\right)\right]\sin(kx)}{D\pi\mu^2\left[s\left(e^{\mu d} + 1\right) + \mu\left(e^{\mu d} - 1\right)\right]} \tag{22}$$

where $\mu = (k^2+\lambda^2)^{1/2}$. Then the current collected shall be,

$$I_{tot} = \int_0^\infty \frac{\partial^2 q(x,z)}{\partial z^2}\bigg|_{x=0} \partial z = \int_0^d \partial z \int_0^\infty ka(k,z)\partial k \tag{23}$$

where z is bound by d, the thickness in z. This in turn gives a total collected current that is a function of sample thickness. Taking the integral over z first,

$$I_0 = \int_0^\infty \frac{\left[s\left(e^{\mu d} + 1\right) + \left(\frac{\mu - 2s}{\mu d}\right)\left(e^{\mu d} - 1\right)\right]}{\pi\mu\left[s\left(e^{\mu d} + 1\right) + \mu\left(e^{\mu d} - 1\right)\right]} dk \tag{24}$$

We also can normalize x by diffusion length and create a dimensionless parameter for s

$$X = \frac{x}{L_b}; S = sL_b \tag{25}$$

and to include a finite width, w ,we sum over all corresponding n

$$k = \frac{n\pi}{w} \tag{26}$$

This gives us a final equation for calculating normalized collected current as a function of a normalized beam-junction distance.

$$I_0(X_0) = \left(\frac{\pi}{w}\right)^2 \int_0^\infty \frac{\left[S\left(e^{\mu d}+1\right)+\left(\frac{L_b\mu-2S}{\mu d}\right)\left(e^{\mu d}-1\right)\right]\sin(kX_0L_b)}{\pi\mu^2\left[S\left(e^{\mu d}+1\right)+L_b\mu\left(e^{\mu d}-1\right)\right]}dk \tag{27}$$

Three simulations were plotted for sample thickness of $10L_b$, L_b and $0.1L_b$. The simulations are plotted over the generation volume distance from the junction, normalized by L_b.

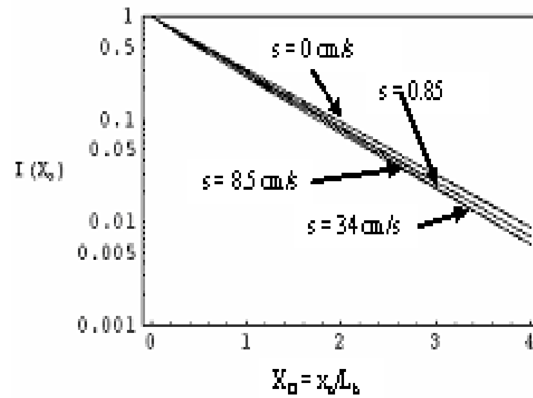

Figure 12. EBIC signal, I(Xo), versus surface recombination velocity, s, for sample thickness of d = 10 Lb.

In Figure 12 we see that for thick samples surface recombination velocity has a small effect on the collected current. Figure 13 is for a sample thickness equal to a single diffusion length, L_b. Here the surface recombination velocity starts to play an important role in the collected current.

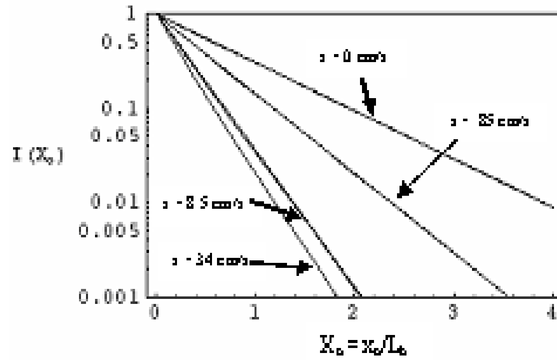

Figure 13. EBIC signal, I(Xo), versus surface recombination velocity, s, for sample thickness of d= 1 Lb.

As can be seen in Figure 13, and more dramatically in Figure 14, small changes in the surface recombination velocity induce significant changes in the collected current profile. This is because minority carriers escaping to the surface recombine, thus not contributing to the collected current. This has the effect of decreasing the sensitivity of EBIC measurements to the diffusion length and allows for increasing resolution. Comparing Figures 12, 13 and 14, one sees that decreasing the sample thickness increases the contribution of non-zero surface recombination velocities.

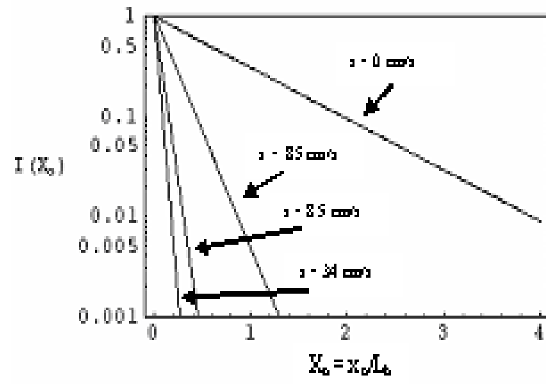

Figure 14. EBIC signal, I(Xo), versus surface recombination velocity, s, for sample thickness of

d = 0.1Lb.

CHAPTER THREE: EXPERIMENTAL METHODS

In order to measure EBIC one must collect the EBIC from the sample device, amplify the current, convert the current to voltage and send the resultant voltage signal to the electronics of the electron microscope for conversion to 2-D contrast images and line scan plots.

Typical electron microscope specimen holders do not provide the transfer of an electrical signal directly from a specimen to an amplifier external to the microscope vacuum chamber. Therefore an EBIC holder was fabricated for the purposes of this research by Dr. Wilber Bigelow, Professor Emeritus, University of Michigan. The EBIC holder provided electrical connection from a sample to an amplifier while maintaining the required vacuum within the microscope vacuum chamber. A picture of this EBIC holder is shown in Figure 15. The external leads of the holder were fitted with a BNC connector for connection to the amplifier.

Figure 15. Specimen holder for EBIC measurements which allows electrical contact between specimen and microscope electronics..

A Stanford Research Systems Model SR570 Low-Noise Current Preamplifier, Figure 16, was used to amplify and convert the EBIC signal to a voltage signal. EBIC signals are typically in the nanoampere range. Therefore the raw EBIC signal must be amplified then sent to scanning microscope electronics for processing. A Stanford Research Systems SR570 Low-Noise Current Preamplifier was used for this purpose. It amplifies the input current and provides and output voltage proportional to the input current. This output signal is compatible with the expected input signal of scanning microscope electronics. The SR570 has a 1 pA/V sensitivity at its lowest sensitivity setting. The SR570 interfaces the TEM or STEM and was used on internal battery power to reduce electromagnetic interference due to ground loops. Output sample images are correlated to EBIC signals. This allows determination of PN junction location or channel length from a defined reference point on the sample. The output of the SR570 preamplifier was connected to the bright field detector output of the FEI Tecnai F30 TEM, Figure 17.

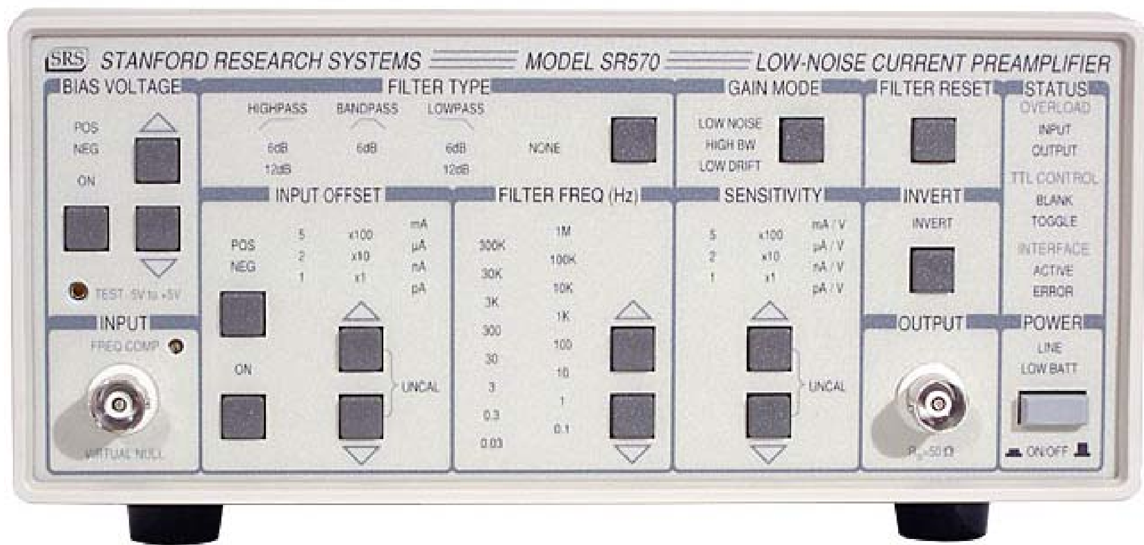

Figure 16. Stanford Research Systems Model SR570 Low-Noise Current Amplifier.

Figure 17. FEI Tecnai F30 TEM. (Photo courtesy of FEI company).

A typical EBIC measurement set-up is provided in Figure 18.

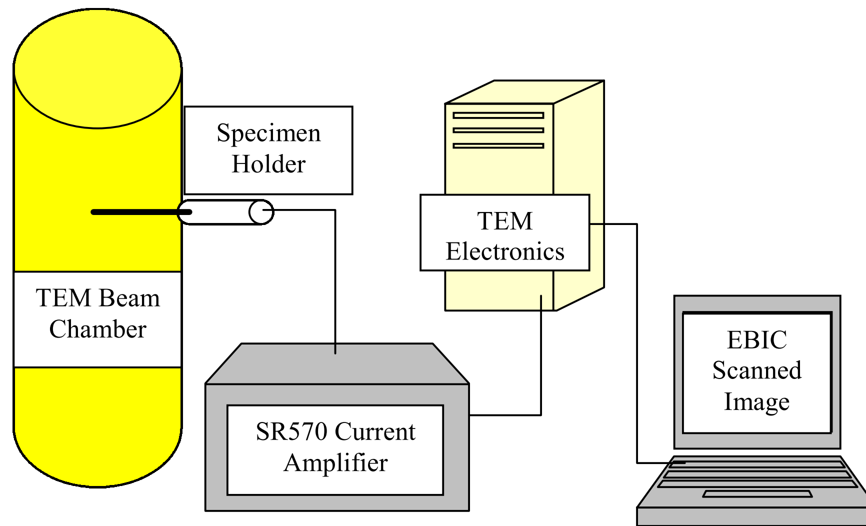

Figure 18. Typical EBIC measurement configuration.

Initial EBIC measurements were performed using diodes made from boron/phosphorus doped Si. Uniformly doped p-type (boron) Si wafers were diffusion-doped with phosphorus to achieve a PN junction. The phosphorus impurity profile was produced by a constant-source diffusion pre-deposition then a limited-source diffusion drive-in. An oxide thickness of 0.3 μm was estimated as the SiO_2 to mask phosphorus [51]. The process schedule is provided in Table 2.

Table 2. Process schedule for diode fabrication.

Process Step	Time	Temperature	Comments
1. Predep. Mask Growth	60 min.	1100° C	Wet O_2 ambient. Estimated 0.45 μm oxide thickness [34]
2. Oxide Etch Mask	20 min.	100° C	Spin-on positive PR, bake
3. Oxide Etch	11 min.		BOE etch oxide off polished side of wafer
4. Phosphorus Predep.	5 min push 20 min soak 5 min pull	935° C	Solid P source, N_2 ambient – 5 psi, flow = 5
5. Drive-In	6 min push 15 min soak 3 min pull	1100° C	
6. Oxide Etch			Acetone remove PR/BOE etch oxide

Next, ohmic contacts were prepared by applying conductive thick film pastes to each side of the wafer. The pastes used, both made by DuPont ®, were Solamet PV202 (4902A) for the p-side of the wafer and Solamet PV143 (4945) for the n-side. The pastes were furnace co-fired in an oxygen environment with an approximate firing profile as provided in Table 3 [52].

Table 3. Process schedule for firing conductive film.

Process Step	Time	Temperature	Comments
1. Fire	75 min.	30° C to 825° C	Dry O_2 ambient
2. Soak	10 min.	825° C	Dry O_2 ambient
3. Cool	90 min.	825° C to 30° C	Room air ambient

Firing of the pastes results in evaporation of solvents, breakdown and decomposition of vehicle polymers, and sintering of inorganic binders and vehicle phase metals [52].

A diffusion profile calculation was performed to estimate the distance of the metallurgical junction from the wafer surface. The pre-deposition, assumed to be solid-solubility limited, drive-in and subsequent firing of thick film paste to form ohmic contacts were incorporated into the impurity profile prediction. The resultant impurity concentration profile follows Fick's second law of diffusion [51]:

$$\frac{\partial N}{\partial t} = D\frac{\partial^2 N}{\partial x^2} \tag{28}$$

where N is the impurity concentration and D is the diffusion coefficient. For a constant-source diffusion of the pre-deposition step, the solution to (28) is:

$$N(x,t) = N_o erfc\left(\frac{x}{2\sqrt{D_1 t}}\right) \tag{29}$$

where N_o is the impurity carrier concentration at the wafer surface, estimated to be $2.6\text{x}10^{20}$ cm^{-3}, the solid-solubility limit at 935° C [53]. D_1 is given by [51]:

$$D_1 = D_o \exp\left[\frac{-E_A}{kT}\right] \tag{30}$$

where D_0 is 10.5 cm^2/sec for phosphorus, E_A is 3.69 eV for phosphorus [51], T is the temperature (K) and k is Boltzmann's constant, giving $D_1 = 4.226 \text{ x } 10^{-15}$ cm^2/sec. From the pre-dep process step we see T = 1208 K and t = 1800 sec, resulting in a Dt product = $7.606 \text{ x } 10^{-12}$ cm^2. The drive-in and the ohmic contact co-fire steps are incorporated into the determination of the final

impurity profile. Using equation (30) the diffusion coefficient for the drive-in step is found to be D_2 = 2.992 x 10^{-13} cm^2/sec. For the co-fire step the temperature in the furnace is time dependent for the fire and cool. Assuming a linear ramp for temperature versus time, T for the fire and cool can be written as:

$$T_3(t) = 0.177t_3 + 303 \tag{31}$$

And for the cool:

$$T_5(t) = -0.147t_5 + 1098 \tag{32}$$

These functions for temperature are used in equation (30) then integrated over the time of each step to determine the diffusion coefficients. For the fire, D becomes:

$$D_3 = \int_0^{4500} D_o \exp\left[\frac{-E_A}{k(0.177t + 303)}\right] dt = 1.942 \times 10^{-14} \frac{cm^2}{\sec} \tag{33}$$

Using equation (30) the diffusion coefficient for the soak is found to be D_4 = 1.212 x 10^{-16} cm^2/sec. For the cool:

$$D_5 = \int_0^{5400} D_o \exp\left[\frac{-E_A}{k(-0.147t + 1098)}\right] dt = 2.211 \times 10^{-14} \frac{cm^2}{\sec} \tag{34}$$

Since the sum of the Dt products for the drive-in and ohmic contact co-fire steps (4.762 x 10^{-10} cm^2) is much greater than that for the pre-deposition step, the final impurity concentration profile due to the drive-in and ohmic contact steps can be approximated by a Gaussian distribution [51] given by:

$$N(x,t) = \left[\frac{Q}{\sqrt{\pi (Dt)_{tot}}}\right] \exp\left[-\left[\frac{x}{2\sqrt{(Dt)_{tot}}}\right]^2\right] \tag{35}$$

where Dt_{tot} is the sum of the Dt products from the drive-in, fire, soak and cool steps Q is the total number of impurity atoms per unit area, or dose, in the silicon as a result of the pre-deposition [51], given by,

$$Q = 2N_o\sqrt{\frac{D_1 t_1}{\pi}} \tag{36}$$

Using D_2, t_2 to designate the drive-in step diffusion coefficient and time, respectively and D_3, t_3, D_4, t_4 and D_5, t_5 for the ohmic contact fire, soak and cool steps, respectively we have $D_2t_2 = 2.693 \times 10^{-10}$ cm^2, $D_3t_3 = 8.739 \times 10^{-11}$ cm^2, $D_4t_4 = 7.273 \times 10^{-14}$ cm^2 and $D_5t_5 = 1.194 \times 10^{-10}$ cm^2 for a $(Dt)_{tot} = 4.762 \times 10^{-10}$ cm^2. The impurity profiles were predicted using MathCad and is presented in Figure 19. The final profile is provided in Figure 20. The resistivity ,ρ, of the (100) boron-doped wafers were measured using a Magne-Tron Model M-700 Resistivity/Conductivity Test System (4-point probe) was found to be 28 Ω-cm. Using this resistivity value and empirical-fit relationship for mobility versus doping concentration given in [53] the boron concentration was calculated to be 4.858×10^{14} cm^{-3}. The metallurgical junction, x_j, as defined as the location where the phosphorus and boron concentrations are equal, was found, using MathCad, to be at 1.426 µm from the wafer surface.

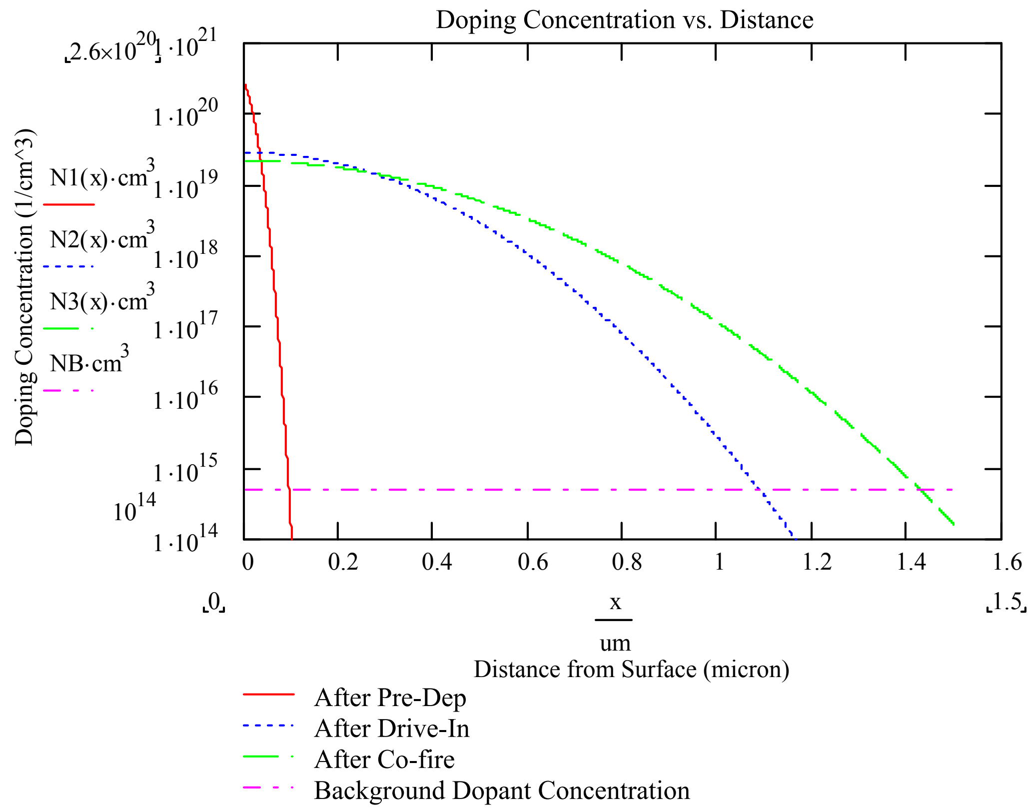

Figure 19. Theoretical impurity concentration profile for fabricated diodes.

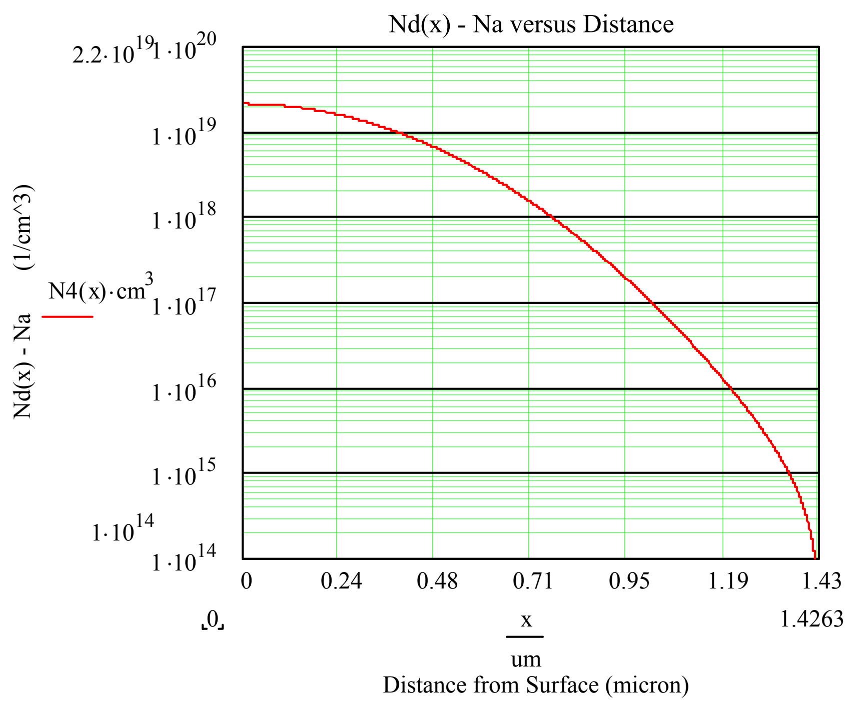

Figure 20. Final theoretical dopant profile, Nd(x) - Na.

The wafer with the ohmic contacts were cut into sections using a South Bay Technology, Inc. Model 650 Low Speed Diamond Wheel Saw with a 3 inch circular blade to sizes adequate for tripod polishing. The diode samples were tripod polished to and angle of approximately 1° to a geometry shown in Figure 20.

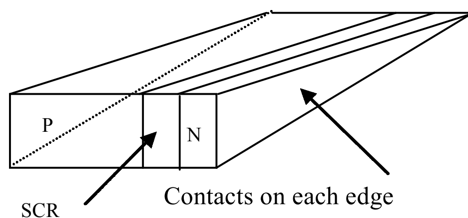

Figure 21. Typical EBIC specimen geometry used in this study.

The diodes were mounted on 3 mm TEM grids using M-Bond 610 Adhesive. A diode sample was then mounted into the TEM EBIC Holder tip using Loctite 408 Instant Adhesive. With 40 AWG wire and Tra-Duct BA-2902 conductive silver epoxy, the ground lead of the TEM EBIC Holder was attached to the n-side of the diode contact and the positive lead was connected to the p-side contact. The sample/holder was then heated to 100°C for 90 min. to cure the epoxy. Current versus voltage was measured to ensure the diode had ohmic contacts and had not been destroyed during the fabrication process. A typical I-V curve for the test samples is given in Figure 22.

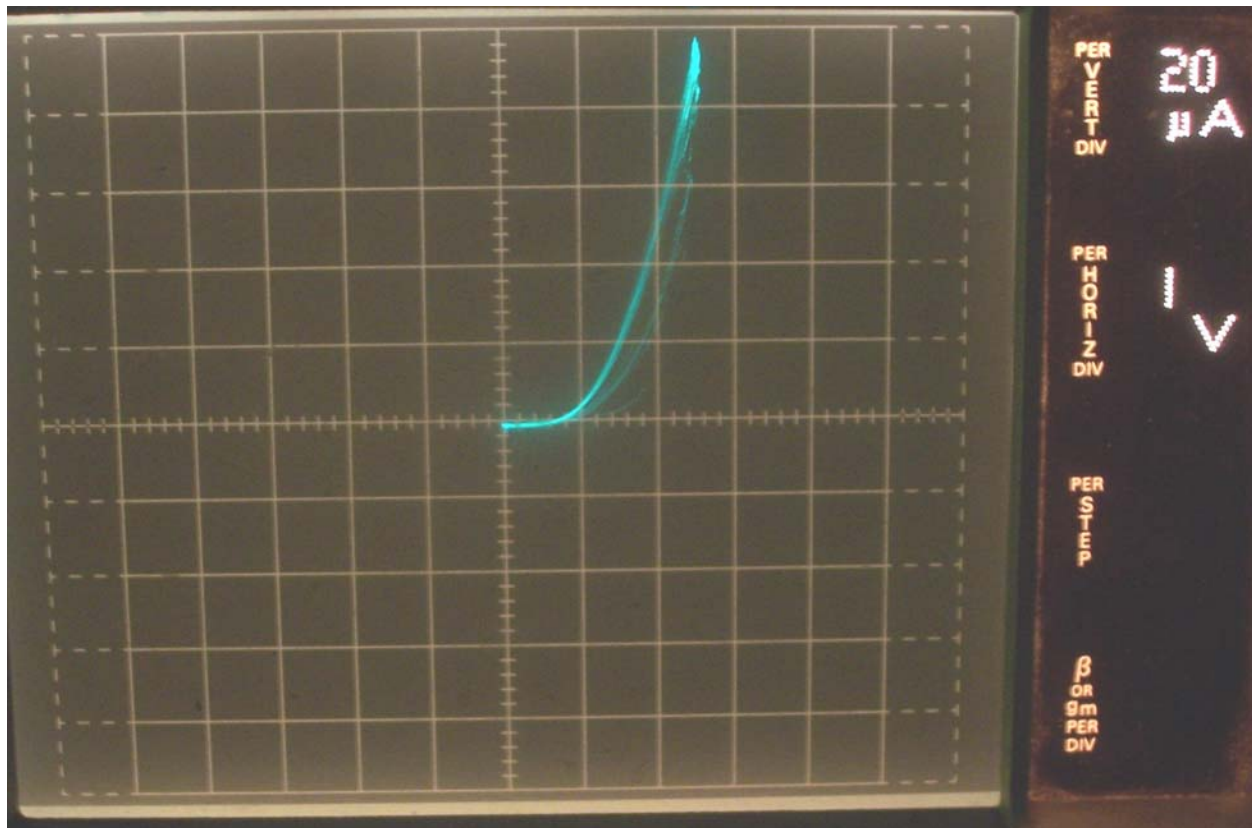

Figure 22. Typical I-V curve for a EBIC specimen diode.

CHAPTER FOUR: RESULTS

The low-noise current amplifier and TEM settings for the EBIC measurements are provided in Table 4 and 5, respectively.

Table 4. Low-noise current amplifier settings.

Setting	**Value**
Bias Voltage	None
Filter Type	None
Filter Frequency	None
Gain Mode	Low Noise
Invert	On
Input Offset	*Variable*
Sensitivity	*Variable*

Table 5. TEM settings.

Setting	**Value**
Probe	Nano
Spot Size	7
MS Exposure Time	*Variable*
Emulsion Setting	2
Extraction Voltage	4300 volts
Gun Lens	5
Mode	LM STEM or STEM
C2 Lens	*Variable*

Figure 23 shows the EBIC measurement setup in terms of signal flow. The diode can be seen on the left side. The EBIC signal (I_{EBIC}) enters the low noise amplifier where a positive or

negative offset can be applied to the signal if desired. The signal can also be inverted (positive or negative) if desired.

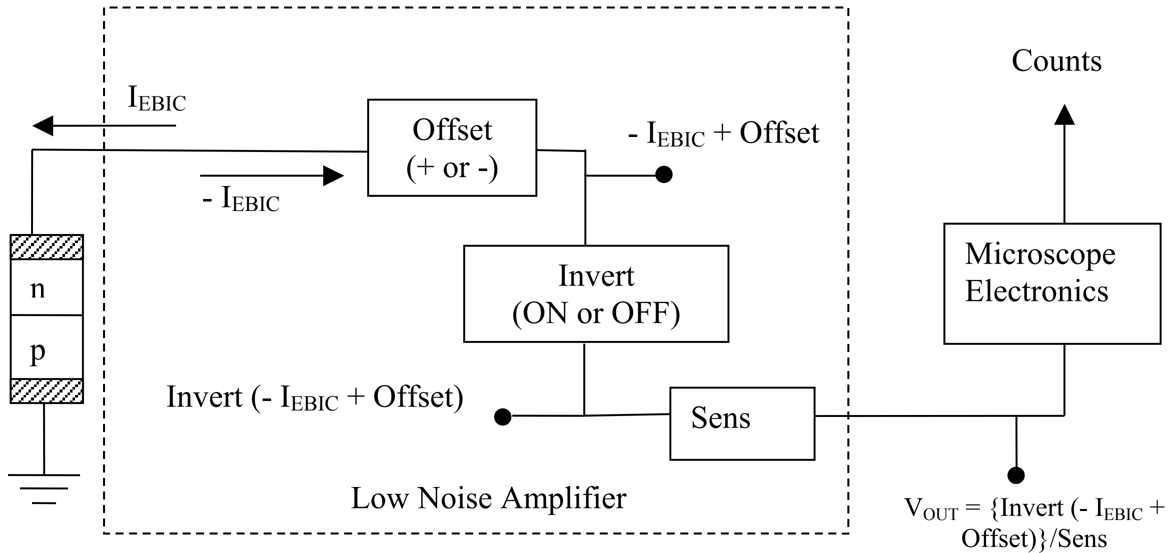

Figure 23. EBIC measurement signal flow.

The sensitivity (Sens) is adjusted by the user so that the EBIC signal can be distinguished but yet not saturate the microscope electronics. As the electron beam is rastered across the area of interest, the output of the microscope electronics is a two-dimensional contrast image where the bright areas refer to relatively larger EBIC current as in Figure 24. A line scan can be produced from the resultant 2-D contrast image as "counts" versus position as in Figure 25. A line is drawn on the contrast image using the line marker tool in the acquisition window of ES Vision.

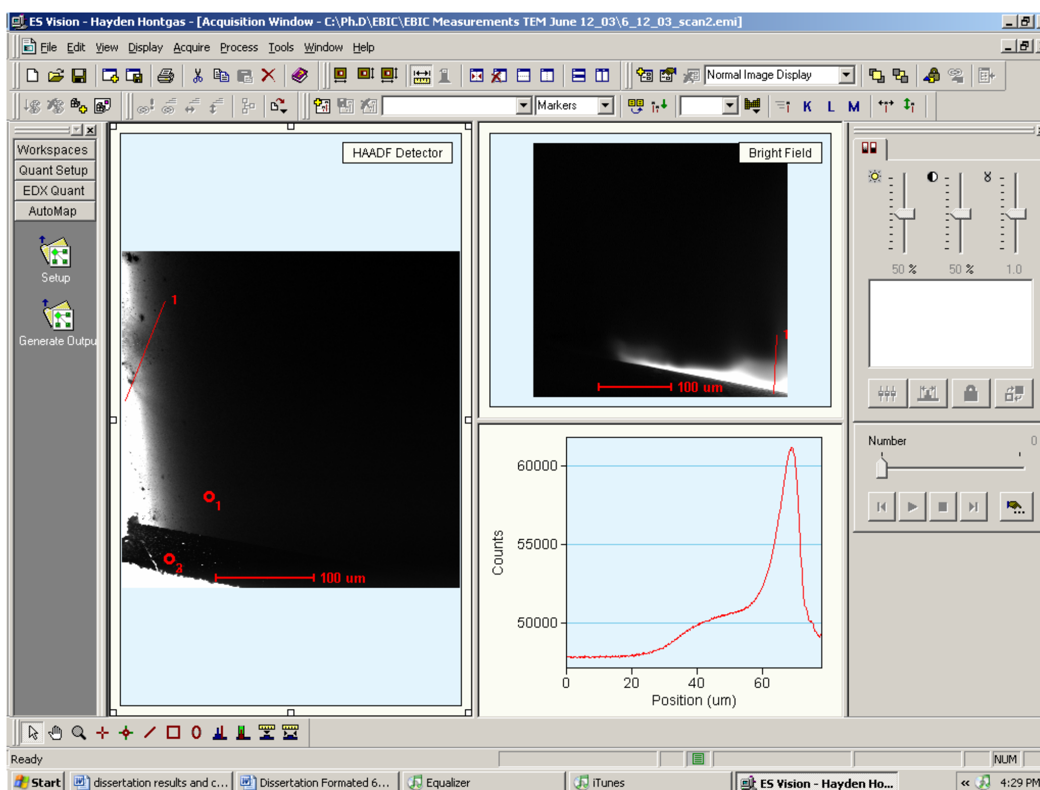

Figure 24. Two dimensional contrast image on left, EBIC image top right, EBIC line scan profile bottom right.

The counts versus position on the line is exported to Excel. “Counts” is an arbitrary unit set by the image brightness but can be referred to current by sending a known current through the Low Noise Amplifier, measuring the output voltage of the Low noise Amp and equating that voltage to the “count” value of the Microscope Electronics output. This was performed several times and the EBIC amplitude was found to typically be a few nA.

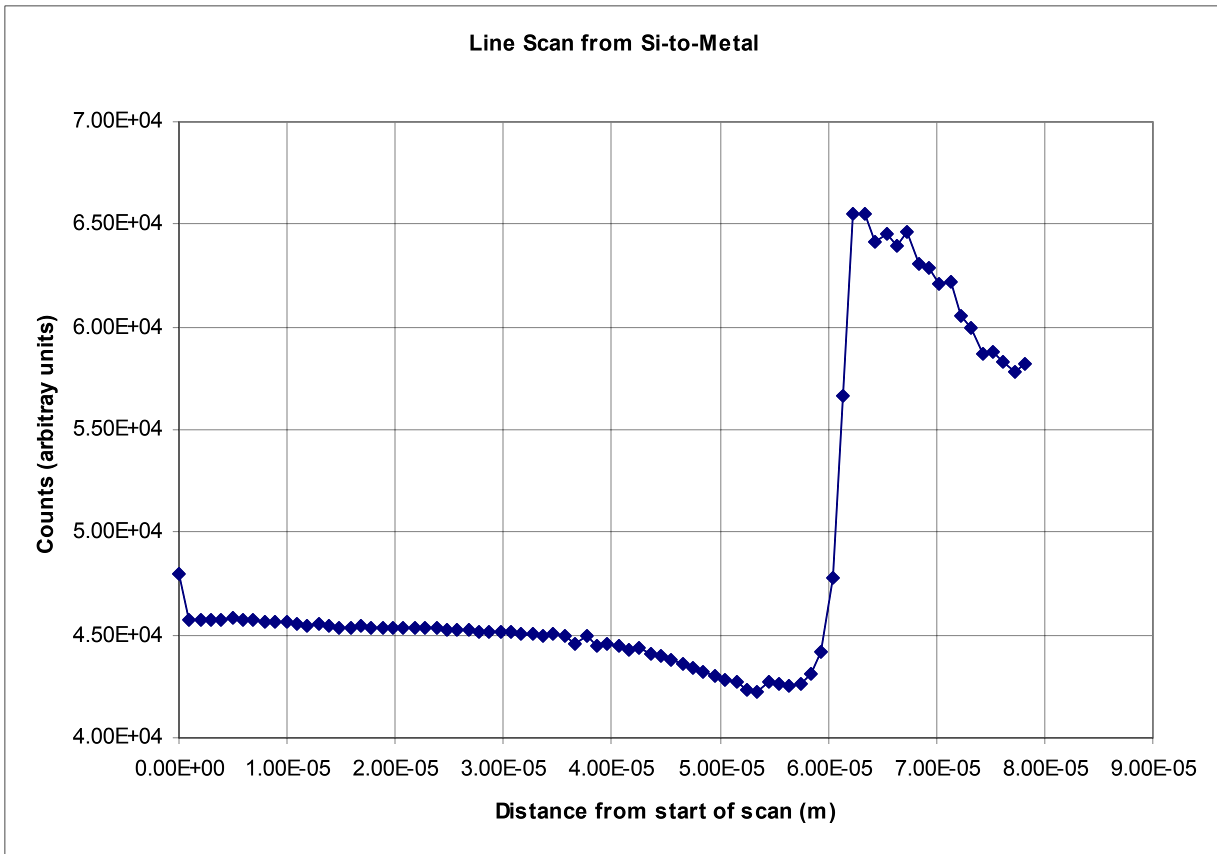

Figure 25. EBIC line scan from contrast image.

Below is the result of a typical TEM image and associated EBIC scan of a wedge-shaped diode.

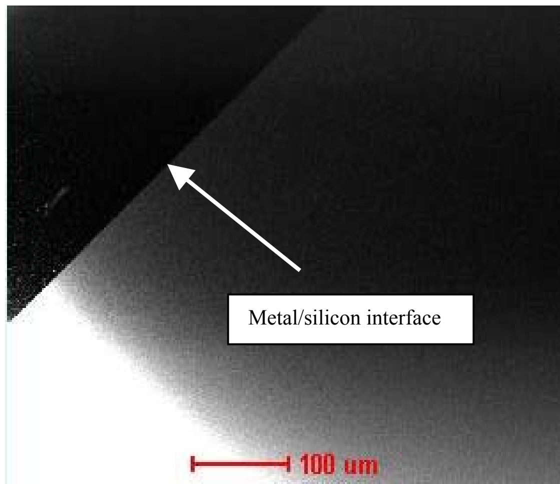

Figure 26. Typical TEM contrast image.

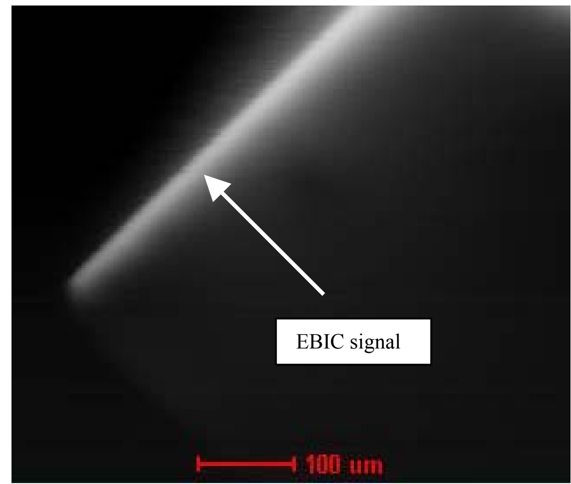

Figure 27. Typical EBIC image.

The dark, top left section of Figure 26 is the metal contact to the silicon diode. Figure 27 shows the EBIC signal (light colored) due to the SCR along the metal/silicon interface. The thinner section of the diode is to the lower left and becomes increasingly thicker toward the upper right. As expected, the EBIC signal can be seen to increase as the diode becomes thicker as seen by the increasing intensity in Figure 27. Figures 28 and 29 are a scan of the same diode but focused on the thin tip.

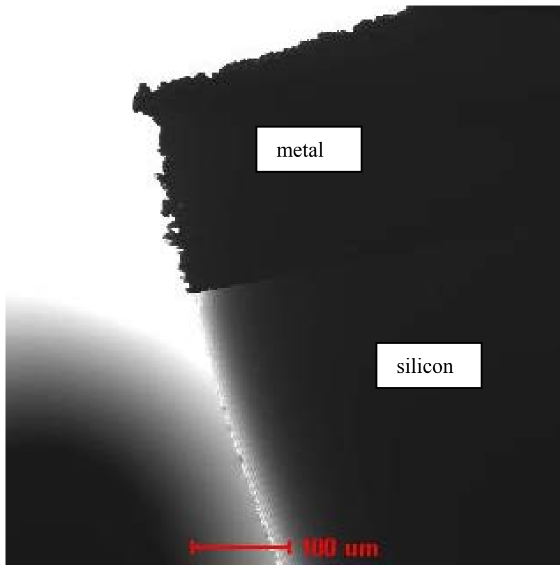

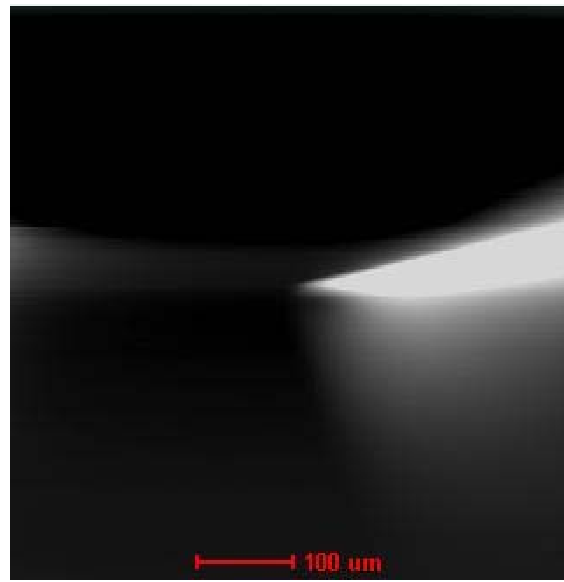

Figure 28. Contrast image of diode tip.

Figure 29. EBIC image of diode tip.

Figure 30 is a plot of the EBIC chosen from an arbitrary thickness (x = 0) within the diode. Increasing distance from this point in the diode corresponds to linearly decreasing thickness. As can be seen from the trend line the EBIC follows a cubic reduction with thickness. A reduction in EBIC signal with decreased thickness is expected as there are fewer atoms available for electron-hole production, and therefore a lower measured EBIC signal. However, no quantitative analysis of measured EBIC signal versus semiconductor device thickness presently exists in the literature.

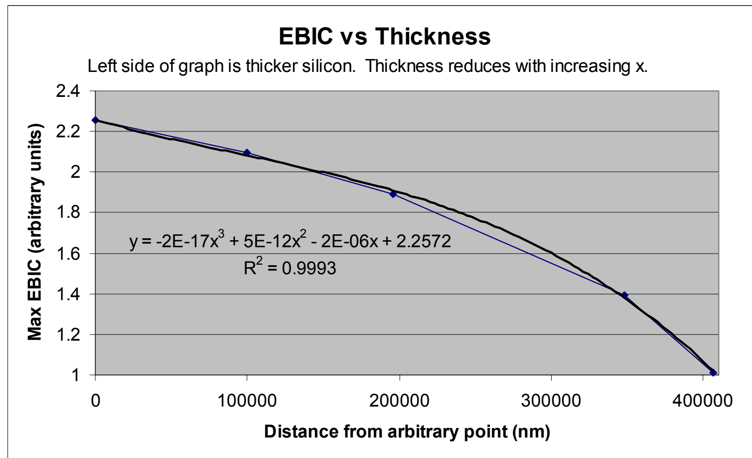

Figure 30. EBIC signal versus diode thickness.

The peak EBIC signal value was determined as a function of the distance from the Si/metal interface for device thickness was found. Figure 31 is a typical result. The x-axis refers to thickness, but the actual values are arbitrary. The y-axis, peak EBIC position, shows true values. As can be seen the peak EBIC signal, which relates to the metallurgical junction, is seen to appear linearly closer to the metal with decreasing thickness, then remains constant at some critical thickness.

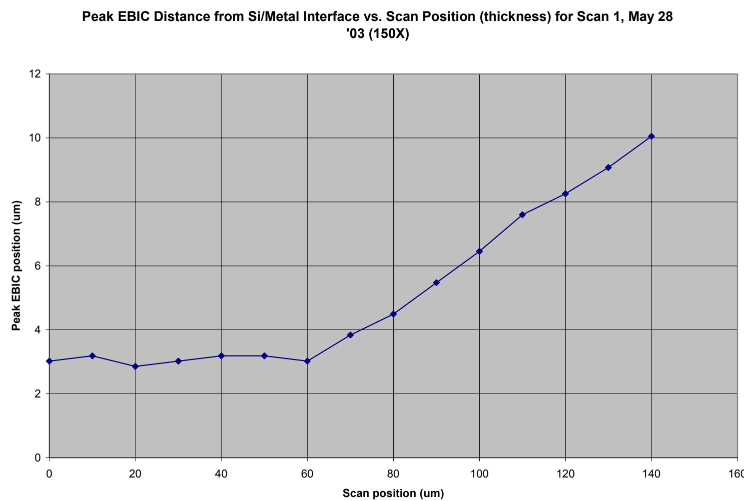

Figure 31. Graph showing EBIC signal versus specimen thickness.

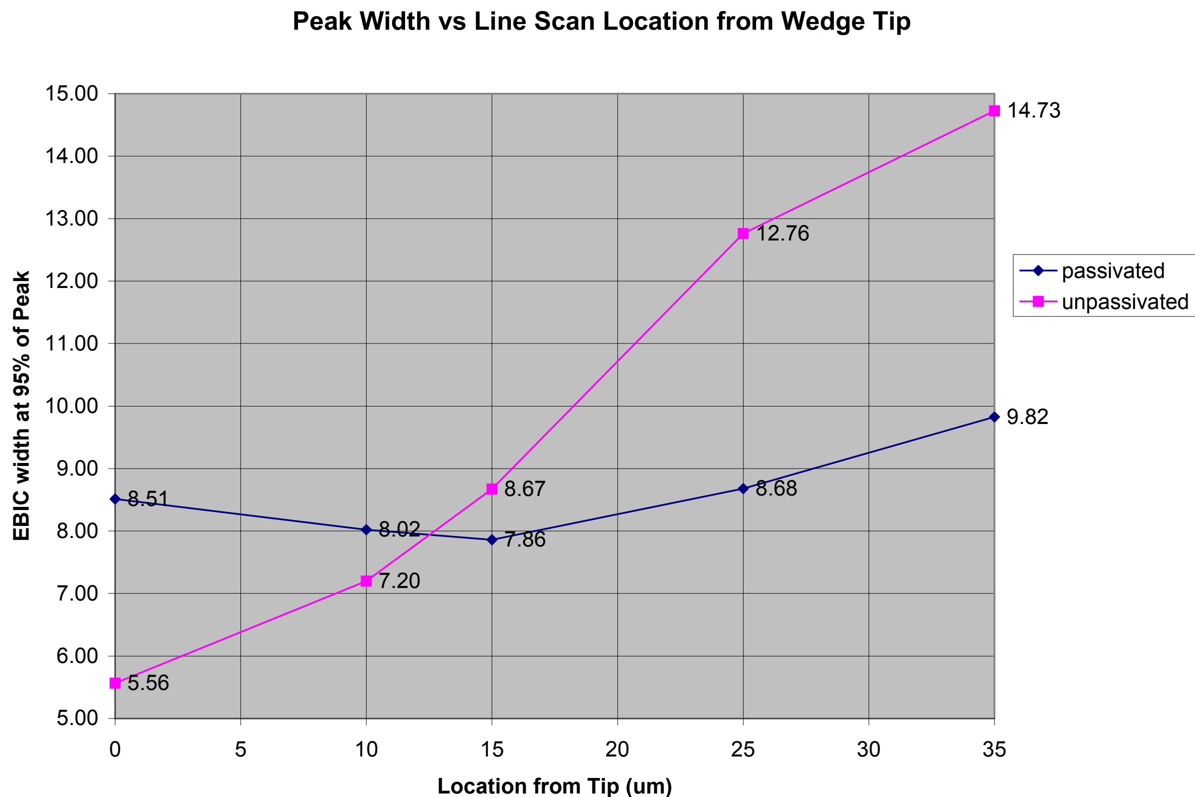

Figure 32. EBIC peak width (95%) versus line scan position from wedge tip.

Figure 31 shows the effect of surface passivation and therefore surface recombination velocity on PN junction delineation resolution. The width of the peak EBIC signal is defined as the distance between the 95% peak values of both sides of the actual peak. So, the smaller the width the higher the resolution to which the PN junction can be defined. The unpassivated curve is for a diode sample for which no surface preparation has been applied. This means the surface contains unattached surface bonds which creates a high surface recombination velocity. The passivated curve is for the same sample that has had surface bonds passivated with a solution of 40 mL of ethanol with 8 drops of HF acid. This has shown to passivate the surface and therefore significantly reduce the surface recombination velocity [46]. As can be seen from the graph, at a

critical device thickness, the high surface recombination velocity causes a trend of a decreasing peak EBIC width and therefore an expected increase in PN junction location resolution.

The effect of surface damage due to the electron beam beyond that produced by the polishing process was observed. Figure 33 shows the diode contrast image on the left with the results of an EBIC image after the electron beam had been impinging along the vertical line (1) across the SCR for approximately 30 seconds.

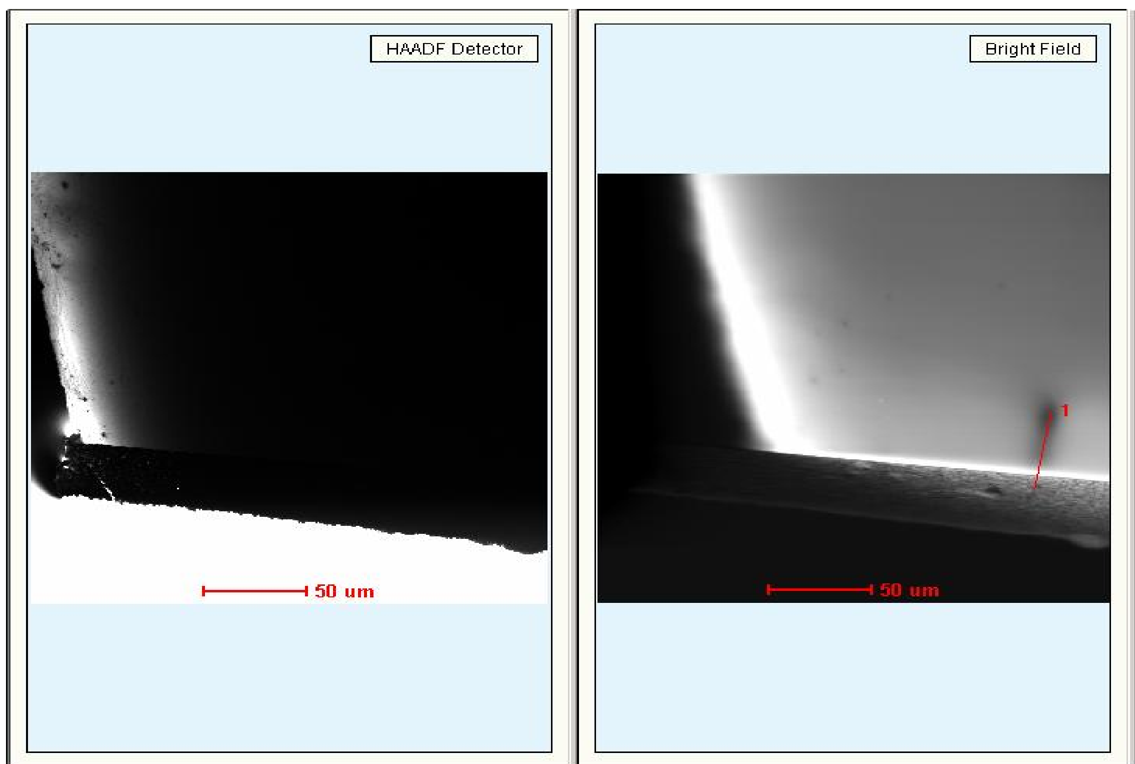

Figure 33. Contrast image (left) and EBIC image (right).

Figure 34 shows a magnified view of the EBIC scan of Figure 33. The image contrast was adjusted to show the effect of the damage of the line scan in Figure 35. As can be seen in Figure 35, the EBIC profile narrowed at the SCR where the line scan was performed. This is believed to be due to the increased surface recombination velocity caused by the line scan. After waiting

approximately 30 minutes before another scan was performed, a subsequent scan showed the damage had vanished and narrowing of the EBIC profile was no longer observed.

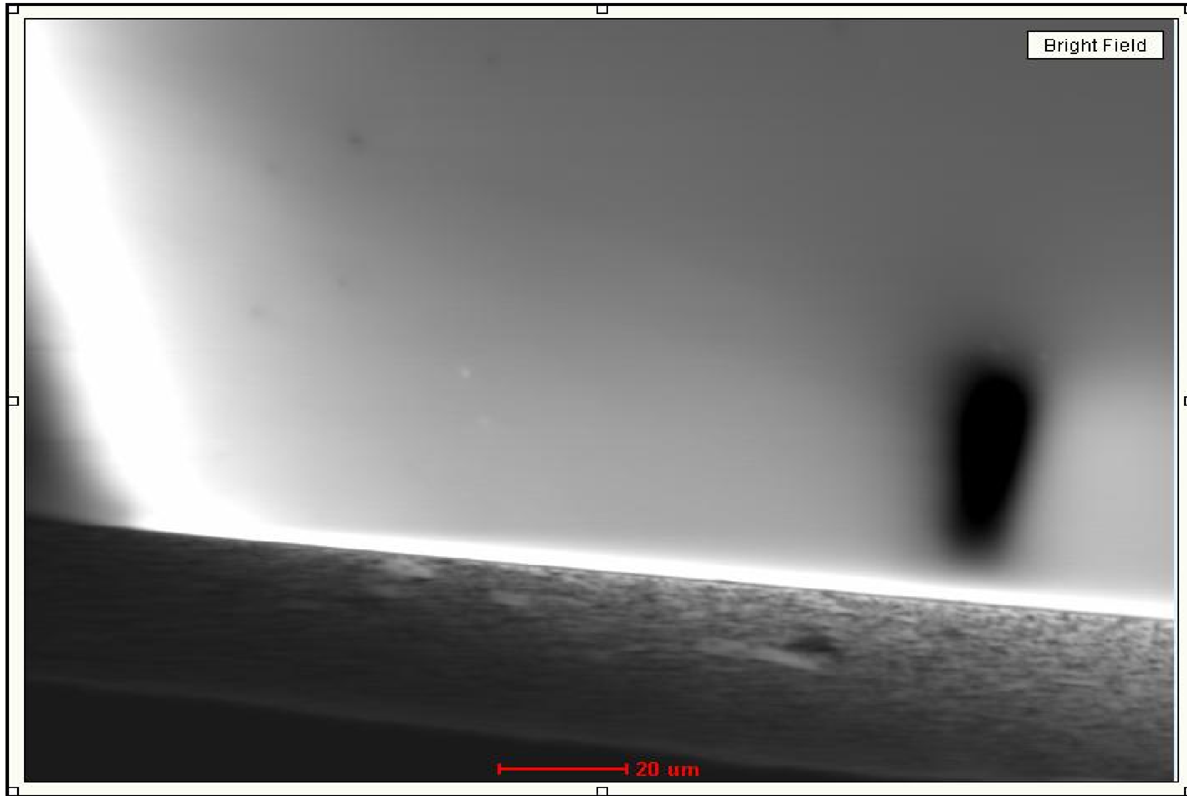

Figure 34. Close-up of damage due to line scan.

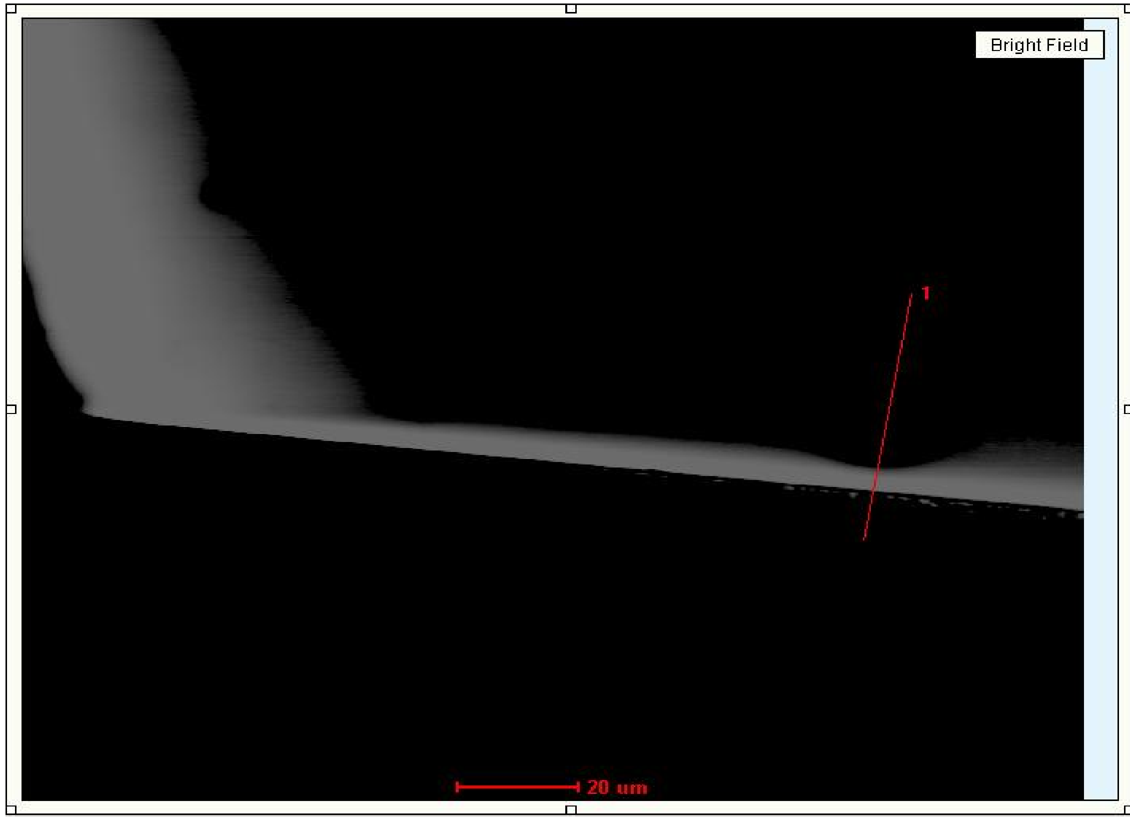

Figure 35. Image enhanced to show narrowing of EBIC profile in damaged region along line scan.

CHAPTER 5: DISCUSSION and CONCLUSIONS

This research has theoretically and experimentally explored the idea of increasing PN junction delineation by utilizing thin semiconductor devices with high surface recombination velocity. This body of work does not exist in the literature. Also new, the EBIC measurements on wedged diode structures with large surface recombination velocity indicate that as the sample thickness decreases the resolution of PN junction delineation increases.

The theoretical and measured metallurgical junction location agree within 5.3% in some cases. Figure 36 shows an EBIC scan where the red vertical line represents where on the diode the line scan data was taken. Figure 37 shows the EBIC data from this line scan, amplitude versus distance. The line scan begins at the metal-silicon interface, extends through the SCR and into the p-region.

Figure 36. EBIC image showing line scan location.

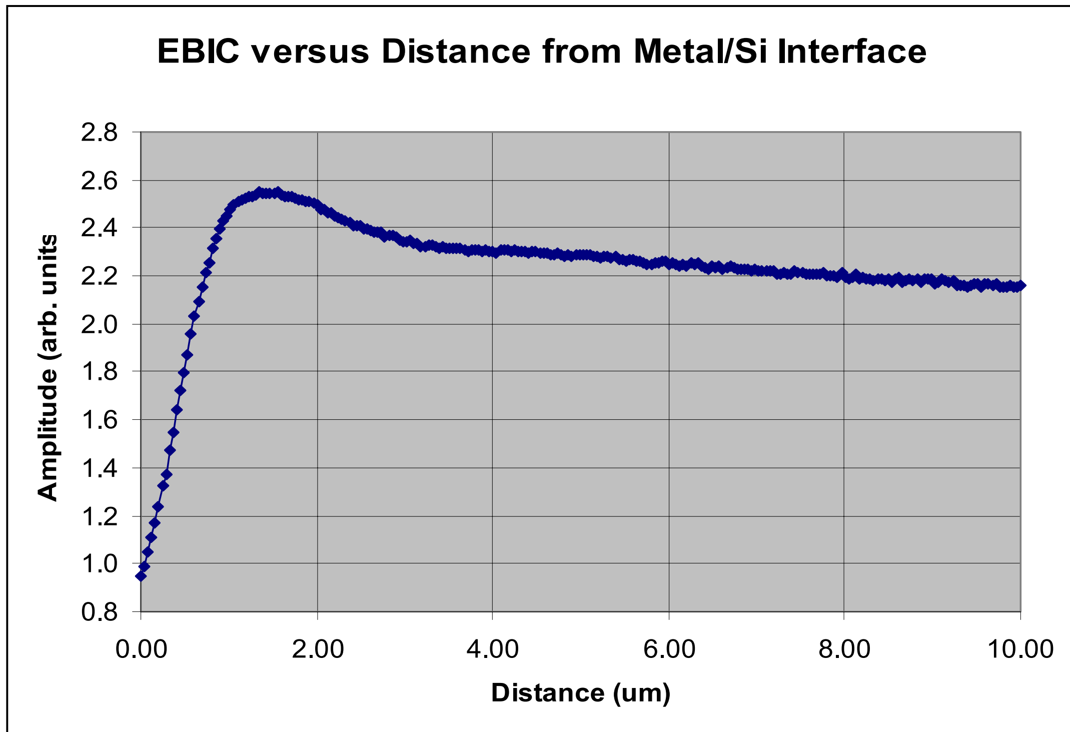

Figure 37. Data from line scan of Figure 33.

The data from this line scan shows the peak EBIC, corresponding to metallurgical junction, occurs at 1.35 µm from the metal-silicon interface. From the theoretical doping profile plots, the metallurgical junction is predicted to be 1.426 µm from the metal-silicon interface. However, as seen in Figure 31 the metallurgical junction, as determined by the distance of the peak EBIC signal from the metal/Si interface, varies with diode thickness after some critical thickness. It is believed that this results from the limit of the generation function delta function approximation used. As the beam moves through some critical thickness, the generation volume is broad enough to exist in the N and P regions as well as the SCR.

As a goal to realize 1 nm resolution, one must obtain an image with 1 nm per pixel. For the Tecnai TEM system, the largest number of pixels per frame is 2048 X 2048.

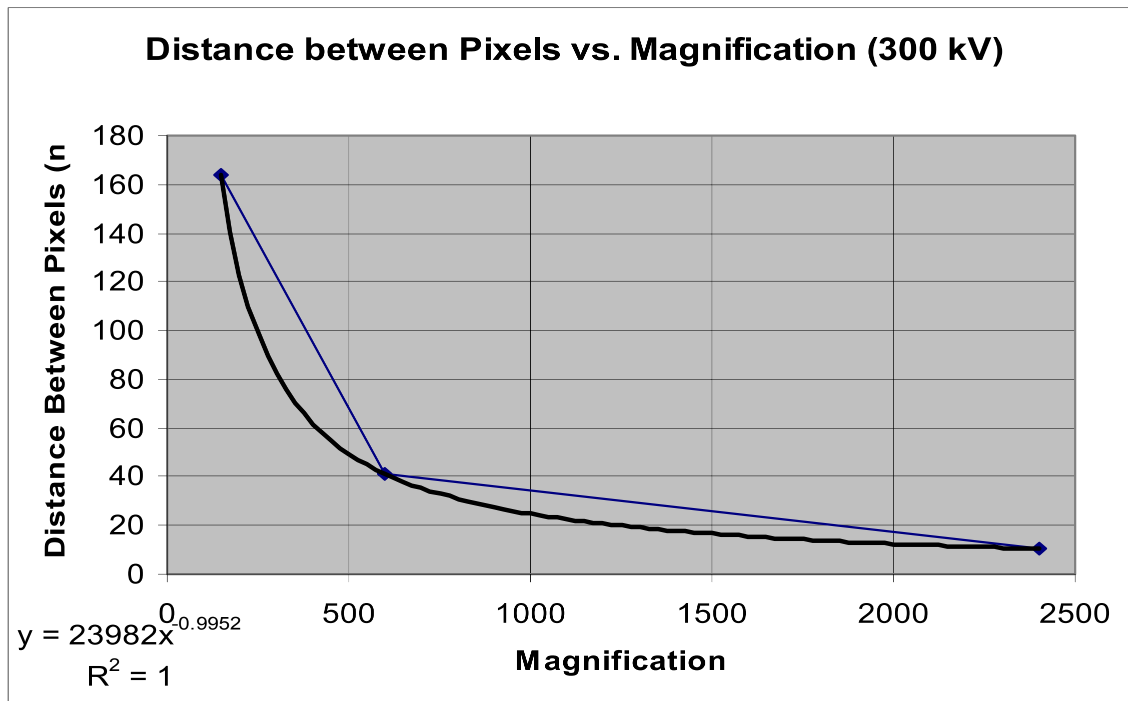

Figure 38. Pixel pitch versus magnification.

Using the TEM analysis software (ES Vision) the pixel pitch versus magnification was determined at magnifications of 150X, 600X and 2400X. Figure 35 shows the graph of these three points with a fit equation of $y = 23982 \times X^{0.9952}$. Using this equation it was found that a minimum magnification of 25200X is required to achieve the required pixel pitch. During this research it was observed that at magnification of 7200X the 300 kV e-beam thermally damaged the silicon. Therefore it was determined to perform measurements with 200 kV e-beam acceleration voltage. The TEM must be aligned and calibrated at each acceleration voltage to be used. The alignment process ensures the optical center of the image coincides with the physical center of the viewing screen, enables optimum focus, minimizes astigmatism and allows a general accurate specimen analysis. Microscope alignments were attempted at 200 kV acceleration voltage but were never adequately achieved. Unfortunately, the FEI Tecnai F30

TEM system used in this research is optimized for operation at 300 kV. Therefore STEM images and EBIC measurements at 200 kV acceleration voltage were of unacceptable resolution to be meaningful to this research.

The largest element of error with this research is in spatial calibration. The accuracy of measured dimensions is dependent on the accuracy of the spatial calibration of the TEM system. To calibrate, a grid pattern of known dimensions, such as in Figure 36, is measured in the STEM mode. Horizontal and vertical lines are drawn along the grid pattern and, based on the grid pattern dimensions, the user inputs the line lengths thus calibrating the microscope. This is a somewhat subjective process in that the user must determine where each line begins and ends.

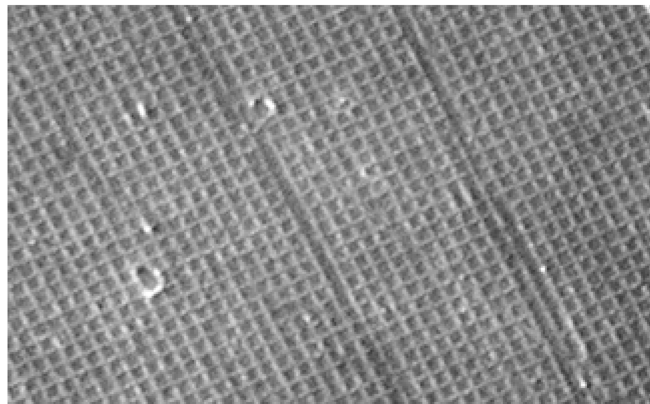

Figure 39. STEM spatial calibration grid pattern.

The user must also ensure the grid is located perpendicular to the electron beam.

To successfully further the research performed here the following is recommended:

1. Beam energies of 200 keV and 100 keV be used to reduce the damage to the semiconducting material yet allow measurable EBIC be generated.

2. A TEM capable of operation with variable beam energies will allow a more complete study of beam energy versus EBIC resolution.
3. As an unexpected result, it was found that the electron beam energy can actually cause damage and increase the surface recombination velocity, which is a desired effect. It is recommended that further study is warranted for use of the electron beam to enhance damage of the semiconductor surface and therefore increase the surface recombination velocity to achieve higher spatial EBIC resolution.
4. It would be desirable to quantify the threshold of damage to doped silicon versus beam energy and current to optimize the surface recombination velocity effect.

Appendix A

EBIC Specimen Rod for
the FEI-Philips F-30 EM

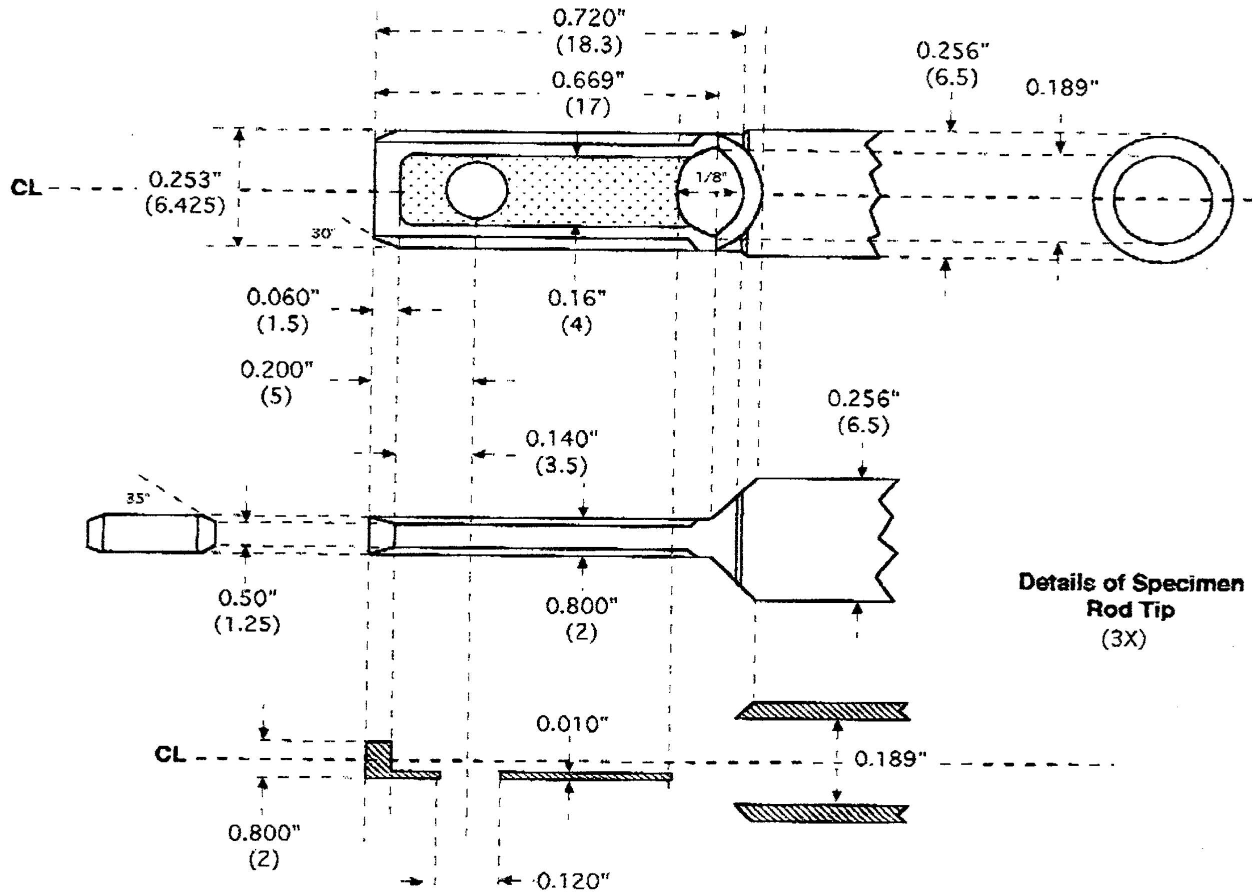

©Wilbur C. Bigelow

Figure A.1. Specimen rod tip.

EBIC Specimen Rod for the FEI-Philips F-30 EM

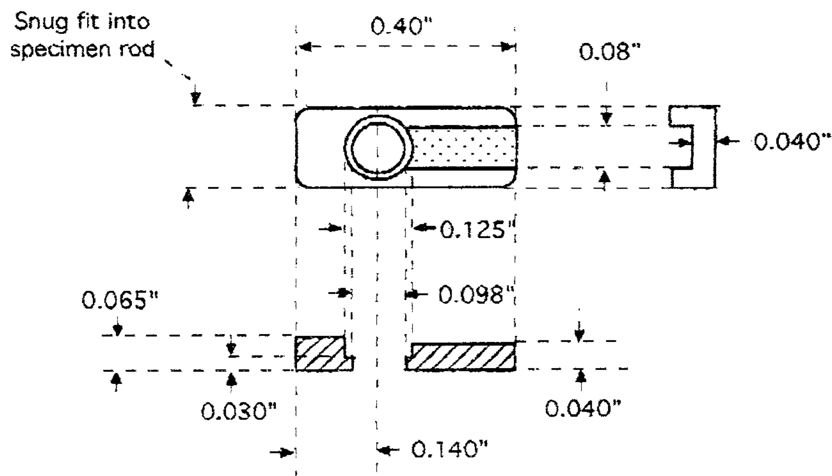

Carrier for Specimen Grid
(Make 3 of Teflon)

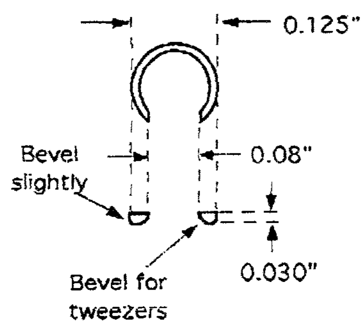

Split ring for holding grid
(make 5 of stainless steel)

©Wilbur C. Bigelow

Figure A.2. Carrier and split ring.

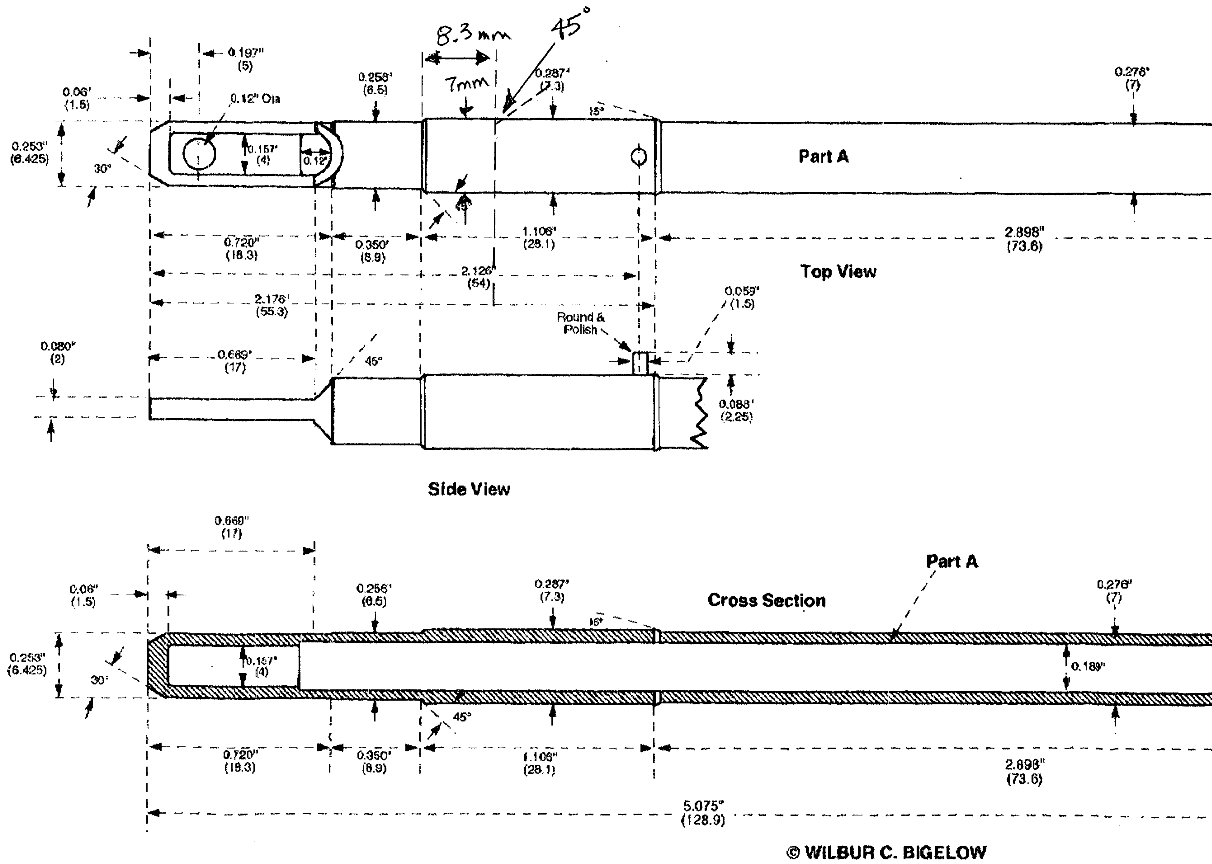

Figure A.3. Specimen rod, section A.

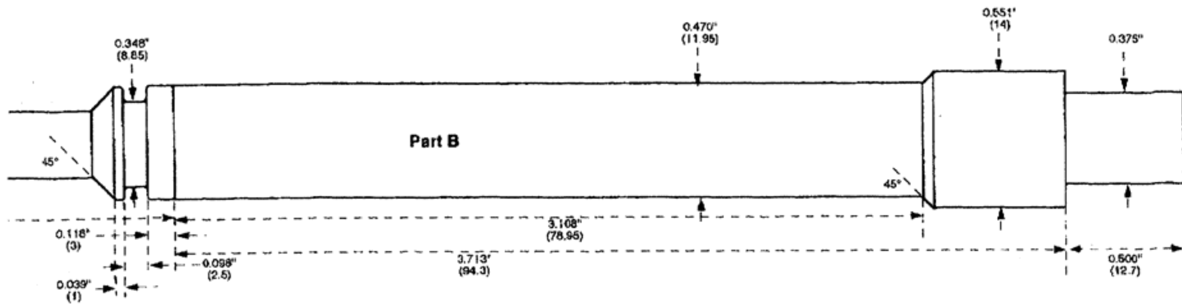

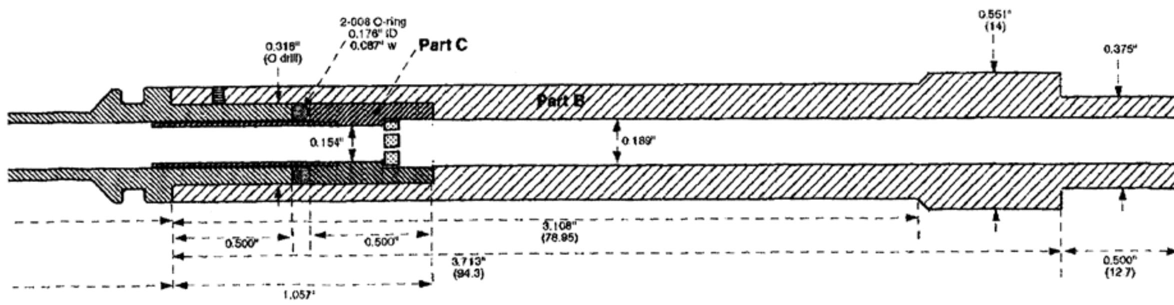

© WILBUR C. BIGELOW

Figure A.4. Specimen rod, section B.

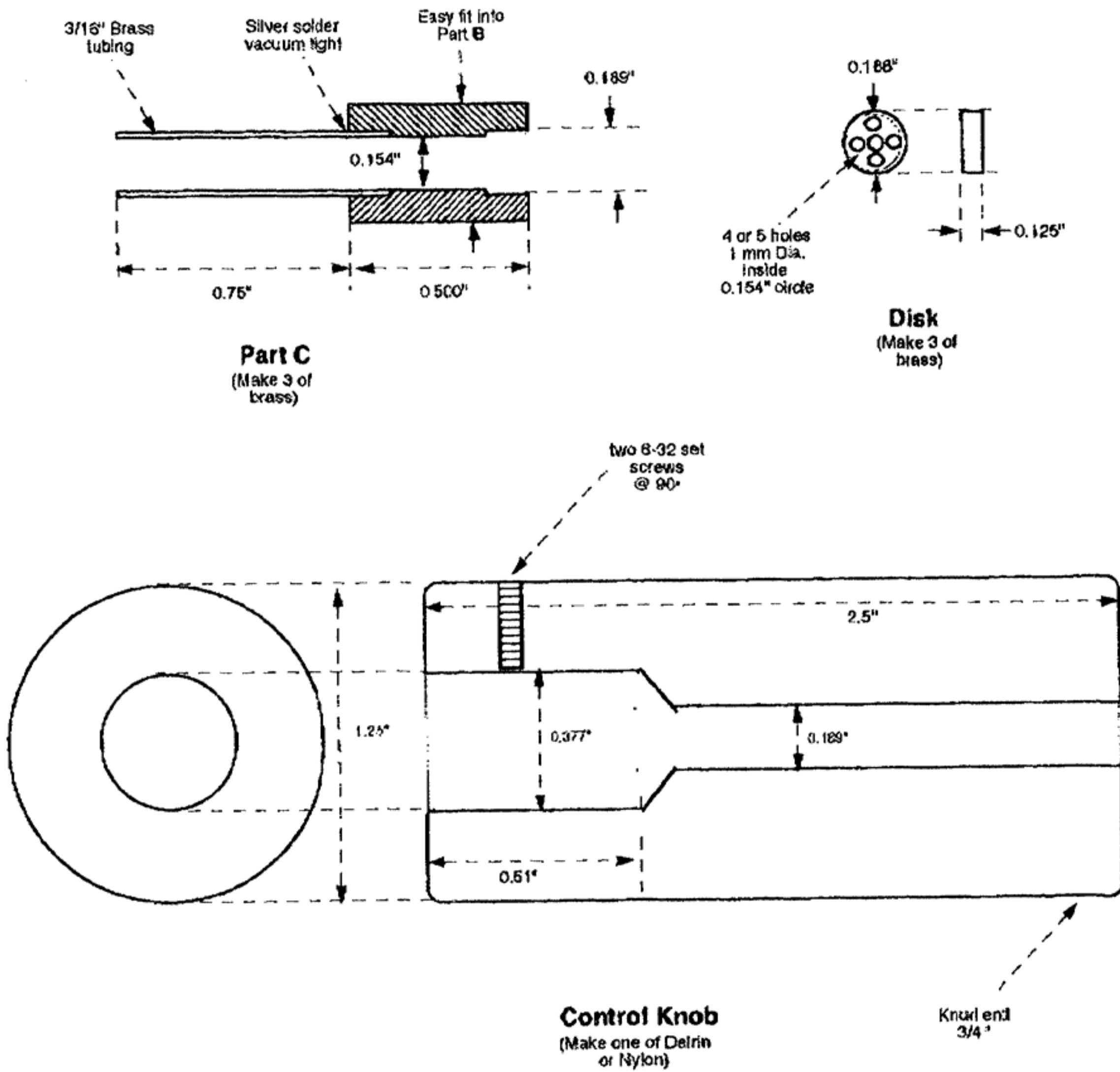

Figure A.5. Specimen rod, section C.

LIST OF REFERENCES

1. L. Jastrzebski, J. Lagowski, H. C. Gatos, "Application of scanning Electron Microscopy to Determination of Surface Recombination Velocity: GaAs," *Applied Physics Letters*, vol. 27, pp. 537-539, Nov. 1975.
2. C. Donolato, "A Method of Analyzing the Induced Current Profiles Obtained on a Schottky Diode at Normal Irradiation," *IEEE Trans. Electron Devices*, vol. ED-31, no. 1, PP. 121-123, Jan. 1984.
3. C. Donolato, "Analysis of Charge-Collection Efficiency Measurements in Schottky Diodes," *Solid-State Electronics*, vol. 31, no. 11, pp. 1587-1594, 1988.
4. B. Sieber, P. Carton, "EBIC Characterization of Bulk GaAs: Temperature Dependence of the Diffusion Length and of the Space-Charge Region Width," *physica status solidi (a)*, vol. 127, issue 2, pp. 423-432, Oct. 1991.
5. G. Oelgart, N. Puhlmann, "Investigation of Minority Carrier Recombination in GaAs: Sn by means of EBIC and CL," *Journal de Physique IV*, vol. 1, pp C6-57 – C6-62, Dec. 1991.
6. E. Grunbaum, E. Napchan, Z. Barkay, K. Barnham, J. Nelson, C. T. Foxon, J. S. Roberts, D. B. Holt, "Evaluation of the Minority Carrier Diffusion Length by means of Electron Beam Induced Current and Monte Carlo Simulation in AlGaAs and GaAs p-i-n Solar Cells," *Semiconductor Science & Technology*, vol. 10, pp. 627-633, May 1995.
7. A. Boudjani, G. Bassou, T. Benbakhti, M. Beghdad, B. Belmekki, "Direct Measurement of Minority Carrier Diffusion Length in Planar Devices," *Solid-State Electronics*, vol. 38, no. 2, pp. 471-475, 1995.

8. G. Jager-Waldau, H. U. Habermeier, G. Zwicker, E. Bucher, “Electron Beam Induced Current Investigations of Active Defects in Silicon due to Reactive Ion Etching and Reactive Ion Beam Etching Processes,” *Journal of Electronic Materials*, vol. 23, pp. 363-367, 1994.

9. D. S. H. Chan, V. K. S Ong, J. C. H. Phang, “A Direct Method for the Extraction of Diffusion Length and Surface Recombination Velocity from an EBIC Line Scan: Planar Junction Configuration,” *IEEE Trans. On Electron Devices*, vol. 42, no. 5, pp. 963-968, May 1995.

10. L. Chernyak, A. Osinsky, H. Temkin, “Electron Beam Induced Current Measurements of Minority Carrier Diffusion Length in Gallium Nitride,” *Applied Physics Letters*, vol. 69, no. 17, pp. 2531-2533, Oct. 1996.

11. JM. Bonard, JD. Ganiere, “Quantitative Analysis of Electron-Beam-Induced Current Profiles Across P-N Junctions in GaAs/$Al_{0.4}Ga_{0.6}As$ Heterostructures,” *Journal of Applied Physics*, vol. 79, no. 9, pp. 6987-6994, May 1996.

12. R. Scheer, M. Wilhelm, L. Stolt, “Temperature Dependent Electron Beam Induced Current Experiments on Chalcopyrite Thin Film Solar Cells,” *Applied Physics Letters*, vol. 70, pp. 1011-1013, Feb. 1997.

13. A. Castaldini, A. Cavallini, A. Poggi, E. Susi, “Surface Damage in Processed Silicon,” *Materials Science and Engineering B*, vol. 42, pp. 249-253, 1996.

14. O. Sjolund, H. T. Lin, D. H. Rich, M. Ghisoni, A. Larsson, S. Wang, J. Thordsson, T. G. Andersson, “Cathodoluminescence and Electron Beam Induced Current Study of Partially Relaxed AlGaAs/GaAs/InGaAs Heterojunction Phototransistors Under

Operating Conditions," *Journal of Applied Physics*, vol. 82, no. 3, pp. 1438-1445, Aug. 1997.

15. Y. Beggah, D. E. Mekki, N. Tabet, R. J. Tarento, "Calculation of the Electron Beam Induced Current at the Interface of a Schottky Contact in the Presence of Shockley-Read-Hall Recombination," *Solid-State Electronics*, vol. 42, no. 3, pp. 379-383, 1998.
16. G. N. Panin, C. Diaz-Guerra, J. Piqueras, "Electron Beam Induced Current and Scanning Tunneling Spectroscopy Correlative Study of $Cd_xHg_{1-x}Te$ and CdTe Crystals," *Semiconductor Science and Technology*, vol. 13, pp. 576-582, 1998.
17. A. Cremades, M. Albrecht, A. Voigt, J. Krinke, R. Dimitrov, O. Ambacher, M. Stutzmann, "Minority Carrier Diffusion Length in AlGaN: A Combined Electron Beam Induced Current and Transmission Microscopy Study," *Solid State Phenomena*, vols. 63-64, pp. 139-146, 1998.
18. C. R. Brennan, M. F. Chriss, C. Taylor, N. M. Haegel, A. M. White, "Electron Beam Induced Current Imaging of Near-Contact Regions in Semi-Insulating GaAs," *IEEE Trans. On Electron Devices*, vol. 45, no. 9, pp. 2024-2031, Sept. 1998.
19. S. Spiga, A. Castaldini, A. Cavallini, M. L. Polignano, F. Cazzaniga, "Denuded Zone and Diffusion Length Investigation of Electron Beam Induced Current technique in Intrinsically Gettered Czochralski Silicon," *Journal of Applied Physics*, vol. 85, no. 3, pp. 1395-1400, Feb. 1999.
20. O. Kruger, M. Kittler, C. Hassler, W. Koch, "Interaction of Crystal Defects with P-N Junctions in Multicrystalline Si Solar Cells," *Solid State Phenomena*, vols. 69-70, pp. 173-178, 1999.

21. V. K. S. Ong, P. C. Liu, K. T. Lau, “Large Area Electron Beam Induced Current Imaging with a Single Contact,” *Solid-State Electronics*, vol. 43, pp. 41-50, 1999.
22. S. Guermazi, A. Toureille, C. Grill, B. El Jani, “Extended Generation Profile – E.B.I.C. Model Application in the Case of a PN Junction,” *The European Physical Journal – Applied Physics*, vol. 9, pp. 43-49, 2000.
23. V. K. S. Ong, K. T. Lau, J. G. Ma, “Theory of the Single Contact Electron Beam Induced Current Effect,” *IEEE Trans. On Electron Devices*, vol. 47, no. 4, April 2000.
24. C. J. Wu and D. B. Wittry, “Investigation of Minority-Carrier Diffusion Lengths by Electron Bombardment of Schottky Barriers,” *J. Appl. Phys.*, vol. 45(5), pp. 2827-2836, May 1978.
25. K.S. Ong and Dethau Wu, “Determination of Diffusion Length from Within a Confined Region with the Use of EBIC,” *IEEE Trans. Electronic Devices*, vol. 48, pp. 332-337, Feb. 2001.
26. C. Donolato, “An Analytical Model of SEM and STEM Charge Collection Images of Dislocations in Thin Semiconductor Layers. I. Minority Carrier Generation, Diffusion and Collection,” *Phys. Stat. Sol. A. Applied Research*, vol. 65, pp. 645-658, June 1981.
27. H.K. Kuiken and C. van Opdorp, “Evaluation of Diffusion Length and Surface Recombination Velocity from a Planar Collector Geometry Electron Induced Current Scan,” *J. Appl. Phys.,* vol. 57(6), pp. 2077-2090, 15 March 1985.
28. V.K.S. Ong, J.C.H. Phang and D.S.H. Chan, “A Direct and Accurate Method for the Extraction of Diffusion Length and Surface Recombination Velocity from an EBIC Line Scan,” *Solid-State Electronics*, vol. 37, no. 1, pp. 1-7, 1994.

29. F.N. Gonzalez and A. Neugroschel, "Measurement of Diffusion Length, Lifetime and Surface Recombination Velocity in Thin Semiconductor Layers," *IEEE Trans. Electron Devices*, vol. ED-31, pp. 413-416, April 1984.

30. Eu. Yakimov, "Electron Beam Induced Current Investigations of Electrical Inhomogeneities with High Spatial Resolution", *Scanning Microscopy*, vol. 6, no. 1, pp. 81-96, 1992.

31. K.L. Luke, O. von Roos and Li-jen Cheng, "Quantification of the Effects of Generation Volume, Surface Recombination Velocity, and Diffusion Length on the Electron Beam Induced Current and its Derivative: Determination of Diffusion Lengths in the Low Micron and Submicron Ranges," *J. Appl. Phys.,* vol. 57(6), pp. 1978-1984, 15 March 1985.

32. D.E. Ioannou and C.A. Dimitriadis, "A SEM-EBIC Minority Carrier Diffusion Length Measurement Technique," *IEEE Trans. Electron Devices*, vol. ED-29, no. 3, pp. 445-450, March 1982.

33. C.A. Dimitriadis, "Determination of Bulk Diffusion Length in Thin Semiconductor Layers by SEM-EBIC," *J. Phys. D: Applied Physics*, vol. 14, pp. 2269-2274, 1981.

34. C.M. Schnabel, M. Tabib-Azar, P.G. Neudeck, S.G. Bailey, H.B. Su, M. Dudley, and R.P. Raffaelle, "Correlation of EBIC and SWBXT Imaged Defects and Epilayer Growth Pits in 6H-SiC Schottky Diodes," *Materials Science Forum*, vols. 338-342, pp. 489-492, 1999.

35. W. van Roosbroeck, "Injected Current Carrier Transport in a Semi-Infinite Semiconductor and the Determination of Lifetimes and Surface Recombination Velocities," *Journal of Applied Physics*, vol 26, no. 4, pp. 382-391, April 1955.

36. F. Berz, H. K. Kuiken, “Theory of Life Time Measurements with the Scanning Electron Microscope: Steady State,” *Solid-State Electronics*, vol. 19, pp. 437-445, 1976.

37. C. Donolato, “Spatial Resolution of SEM-EBIC Images,” *Solid-State Electronics*, vol. 22, pp. 797-799, 1979.

38. D. E. Ioannou, S. M. Davidson, “Diffusion Length Evaluation of Boron-Implanted Silicon using the SEM-EBIC/Schottky Diode Technique,” *Journal of Physics D: Applied Physics*, vol.12, pp. 1339-1344, 1979.

39. G. E. Possin, C. G. Kirkpatrick, “Electron-Beam Measurements of Minority-Carrier Lifetime Distributions in Ion-Beam-Damaged Silicon,” *Journal of Applied Physics*, vol 50(6), pp. 4033-4041, 1979.

40. B. Akamatsu, J. Henoc, P. Henoc, “Electron Beam-Induced Current in Direct Band-Gap Semiconductors,” *Journal of Applied Physics*, vol. 52(12), pp. 7245-7250, 1981.

41. Oldwig von Roos, Keung L. Luke, “Analysis of the Interaction of an Electron Beam with Back Surface Field Solar Cells,” *Journal of Applied Physics*, vol. 54(7), pp. 3938-3942, 1983.

42. T. V. Rao, V. Dutta, O. S. Sastry, K. L. Chopra, “Electron Beam Induced Current Technique Using a Scanning Auger Microprobe,” *Review of Scientific Instruments*, vol. 55, pp. 1129-1131, 1984.

43. Dethau Wu, Vincent K. S. Ong, “Determination of Material Parameters from Regions Close to the Collector using Electron Beam-Induced Current,” *IEEE Transactions on Electron Devices*, Vol. 49, no. 8, pp. 1455-1461, August 2002.

44. M. Kittler and J. Larz, “Evaluation of p-n Junction Position and Channel Length in Si Devices with Resolution of a Few Nanometers by Low-Energy EBIC,” *Solid State Phenomena*, vol. 63-64, pp. 77-88, 1998.

45. Carl E. Norman, “Challenging the Spatial Resolution Limits of CL and EBIC,” *Solid State Phenomena*, vol. 78-79, pp. 19-28, 2001.

46. Gerald W. Neudeck, *Modular Series on Solid State Devices, Volume II: The PN Junction Diode*, Reading Massachusetts, Addison-Wesley Publishing Company, 1989, pg. 37.

47. R. Kuhnert, “Electron Beam Induced Current Images of Sectioned P/N Junctions in Silicon: Influence of Surface States at Low Acceleration Voltages,” Journal of Applied Physics, vol. 71(1), pp. 476-484, 1 July 1991.

48. H. J. Leamy, “Charge Collection Scanning Electron Microscopy,” J. Appl. Phys., vol. 53(6), pp. R51-R80, June 1982.

49. T.E. Everhart and P.H. Hoff, ”Determination of Kilovolt Electron Energy Dissipation vs. Penetration Distance in Solid Materials,” Journal of Applied Physics, vol. 42(13), pp. 5837-5846, December 1971

50. C. Donolato, “On the Analysis of Diffusion Length Measurements by SEM,” Solid-State Electronics, vol. 25, no. 11, pp. 1077-1081, 1982.

51. Richard C. Jaeger, *Modular Series on Solid State Devices, Volume V: Introduction to Microelectronic Fabrication*, Reading Massachusetts, Addison-Wesley Publishing Company, 1993, pg. 60.

52. Trevor R. Allington, “Thick Film Processing for Higher Yields – Part Two: Furnaces and Firing,” *DuPont Co., Electronics Materials Div., Hybrid Circuit Workshop.*, Lake Publishing Corporation, Libertyville, IL, Apr. 1982.

53. Robert F. Pierret, *Modular Series on Solid State Devices, Volume VI: Advanced Semiconductor Device Fundamentals*, Reading Massachusetts, Addison-Wesley Publishing Company, 1989, pg. 188.